Reprinted from ANNALS OF PHYSICS

Vol. 94, No. 1, September 19, 1975
Printed in Belgium

On the Valence Model for Radiative Capture

J. CUGNON*

Institut de Physique Nucléaire, Division de Physique Théorique, 91406 Orsay, France

AND

C. MAHAUX

Theoretical Physics, University of Liège at Sart Tilman, 4000 Liège 1, Belgium

Received April 22, 1975

We give several parametrizations for the elastic scattering and radiative capture cross sections for low neutron bombarding energy and discuss the relationship between the corresponding resonance parameters. We then perform an extensive investigation of the valence radiative capture model of Lane and Lynn. This model is formulated here in the frame of the shell-model approach. We exhibit the similarities and differences between our results and those derived from the R-matrix approach by Lane and Lynn on the one hand and from the optical-model approach by Lane and Mughabghab on the other hand. Particular attention is paid to the choice of the average potential well in the shell-model approach, in relation to the proper way to identify theoretical quantities and phenomenological parameters. We show that practically equivalent results can be obtained from a complex average potential well and from a suitably chosen real potential well, respectively. The following topics are investigated formally and numerically: dependence of the various theoretical expressions on the choice of the (real or complex) average potential well; relative importance of external and internal capture; dependence of photon widths and background cross section on mass number (for thermal energy and for $E = 100$ keV); dependence of the resonance parameters and background cross sections on energy, for $A = 60$; comparison between experimental data and theoretical values for radiative capture on ^{56}Fe and ^{60}Ni. We discuss the conditions of validity of the valence capture model. In particular, we investigate the role of the giant dipole resonance and of the closed channels. We argue that the success of the valence capture model is intimately related to the importance of external capture. The contribution of the low-lying excited target states is investigated formally and numerically; it increases with mass number and tends to diminish the correlation between neutron and photon widths, which is implied by the valence capture model.

* On leave from University of Liège, Belgium.

1. Introduction

Recently, theoretical interest in the radiative capture of low-energy neutrons has been strongly enhanced by the accumulation of experimental evidence for deviations from the standard statistical assumptions. These phenomena have been interpreted in the frame of the valence capture model of Lane and Lynn [1–4]. In their pionneering work, these authors used the R-matrix theory of nuclear reactions. Most analyses and theoretical contributions have since been carried out in that formalism. The main purpose of the present paper is threefold: (1) In view of the current interest in another approach to nuclear reaction theory [5, 6], it is desirable to investigate how the valence capture model can be formulated in that framework, and the relationship between the corresponding results and the work by Lane and Lynn [1–4]. We show formally and numerically that under suitable conditions all formulations lead to the same results. (2) We investigate in some detail the main physical predictions and characteristic features of the valence capture model. (3) We study the origin of the validity of the valence capture model. In particular, we investigate the role of the closed channels and of the giant dipole resonance. We illustrate the discussion of these three main topics by numerical examples in the region $40 < A < 80$.

Our discussion is centered on the shell-model approach to nuclear reactions [5], which is closely related to Feshbach's unified theory [6]. The formal extension of these theories to the discription of photonuclear reactions was carried out in [7–9], and (partly misleading, see Section 3) numerical results concerning radiative capture at low energy have been given in [10, 11]. Some important questions remained unanswered by these papers. In particular, the mutual relationship between the R-matrix [1–4], the optical-model [12], and the shell-model expressions [5–11] has not yet been discussed in detail. In particular, the following problem exists, as recently emphasized by Lane and Mughabghab [12]. In [10, 11], the background and resonance parameters have been calculated from a real average single-particle potential. This appears to be at variance with the original prescription of Lane and Lynn [2–4], which involves a complex optical-model potential. Recently, a (largely) framework-independent derivation of the Lane-Lynn result has been given [12]. Hence, it appears necessary to study under what conditions the shell-model expressions, which at low energy involve a real potential well, are compatible with those of Lane, Lynn, and Mughabghab [1–4, 12]. The understanding of this point is of intrinsic interest, since the use of a complex potential at low energy does not appear to be necessary in view of the facts that the inelastic channels are closed and no average over energy is taken.

The present paper is organized as follows.

(1) We discuss, in Section 2, the relationship between several parametrizations for the elastic scattering and radiative capture cross sections at low energy.

This is of interest for three related reasons: (a) Apparent differences between theoretical formulas for the "partial widths" may simply reflect the fact that the expression "partial width" is associated with different quantities. (b) The identification between theoretical resonance parameters and phenomenological values implies that both refer to the same parametrization. (c) The statistical properties of the resonance parameters are in general sensitive to their detailed definition. The latter point was emphasized by Feshbach [13], who wrote that "one must bear in mind how the data were analyzed and in particular how the potential scattering was described." We will see that radiative capture at low energy offers a very instructive illustration of this warning.

(2) In Sections 3.1–3.4, we formulate in the shell-model approach the valence capture model of Lane and Lynn [2–4]. The content of these sections completes some results given in [11]. In particular, we compare the shell-model and R-matrix expressions, and we usually consider the K-matrix rather than the S-matrix parametrization. These sections also contain an improvement of a numerical (factorization) approximation made in [11], which turns out to be grossly inaccurate in the calculation of the (most important) contribution of the surface region to the capture process.

(3) In Section 3.5, we discuss the connection between the complex optical-model potential and the results derived in Sections 3.1 and 3.3, which involve a real potential well. The problem of the best choice of the latter single-particle potential is discussed: It is intimately related to Feshbach's remark ([13] cited above).

(4) In Section 4, we give a number of numerical results, with four main aims in mind. (a) We compare theoretical and experimental values for the photon widths in the cases $^{56}Fe(n, \gamma)$ and $^{60}Ni(n, \gamma)$. (b) We investigate and illustrate a number of relationships discussed in the preceding sections. (c) We study the dependence of the calculated partial widths and of the theoretical background cross section on the choice of the (complex or real) single-particle potential. (d) We show the dependence on mass number of the photon width $\Gamma_{\lambda f}$ and of the ratio $\Gamma_{\lambda f}/\Gamma_{\lambda n}$, where $\Gamma_{\lambda n}$ is the partial width in the neutron channel, for thermal energy and for $E = 100$ keV, respectively.

(5) In Section 5, we investigate the dynamical origin of the success of the valence capture model near the peaks in the neutron strength function. In particular, we study the relative importance of the closed channels and of the giant dipole resonance. We show that the external capture and the dependence of the scattering length on mass number play a central role in the understanding of the conditions of validity of the valence capture model.

2. Parametrizations

In the present section, we study the relationship between several parametric forms for the collision matrix. We restrict (see, however, Section 2.4) the discussion to the case of only one open particle channel (s-wave neutron) and neglect the damping due to photon channels. In Sections 2.1 and 2.2 we consider parametrizations in terms of the poles and residues of the reactance matrix and of the collision matrix, respectively. Then we turn (Section 2.3) to expressions that involve a model background potential scattering phase shift θ. In the present section, we need not specify the nature of θ; in R-matrix theory, θ usually will be taken as the hard sphere scattering phase shift; in the shell-model approach, θ normally is associated with the phase shift due to some average (real) potential well. In Section 2.4 we discuss the connection that exists between the correlation between photon and neutron partial width amplitudes on the one hand and the average of the scattering matrix on the other hand. The one-level approximation is considered in Section 2.5, Finally, the identification between theoretical and phenomenological resonance parameters is discussed in Section 2.6.

2.1. *Reactance Matrix*

For simplicity, we ignore antisymmetrization and write the scattering wavefunction in the form

$$\Psi_E = r^{-1}u(r; E)\,\psi_t\,, \tag{2.1}$$

where ψ_t is the target wavefunction and r is the radial coordinate of the incoming s-wave neutron. We restrict the discussion to a 0^+ target state and do not write explicitly the spin part of the wavefunction. In the literature, two slightly different normalizations are in current use; they are associated with the following asymptotic behaviors,

$$u^+(r; E) \sim \left(\frac{2}{\pi\hbar v}\right)^{1/2} [e^{-ikr} - S_{nn}e^{ikr}], \tag{2.2}$$

and

$$u(r; E) \sim \left(\frac{2}{\pi\hbar v}\right)^{1/2} [\sin kr + K_{nn} \cos kr], \tag{2.3}$$

respectively, and are related by

$$u^+(r; E) = -2i(1 - iK_{nn})^{-1}\, u(r; E). \tag{2.4}$$

We call d the dipole operator, suitably normalized (see Section 4.1). The reactance matrix $\mathbf{K}$ and the scattering matrix $\mathbf{S}$ are given by

$$S_{nn} = \frac{1 + iK_{nn}}{1 - iK_{nn}}\,, \qquad S_{nf} = \langle \Psi_f \mid d \mid \Psi_E{}^+\rangle, \tag{2.5}$$

$$K_{nf} = -\langle \Psi_f \mid d \mid \Psi_E\rangle, \qquad S_{nf} = \frac{2iK_{nf}}{1 - iK_{nn}}\,, \tag{2.6}$$

where Ψ_f is the wavefunction of the state reached after photon emission. The reactance matrix $\mathbf{K}$ is real.

Lane and Mughabghab [12] assume that one can write

$$K_{nn} = K_{nn}^{(0)} + \frac{1}{2}\sum_\lambda \frac{\Gamma_{\lambda n}}{E_\lambda - E}\,, \tag{2.7}$$

where all quantities are real and independent of energy. From Eqs. (2.4) and (2.5), we find

$$K_{nf} = K_{nf}^{(0)} + \frac{1}{2}\sum_\lambda \frac{\Gamma_{\lambda n}^{1/2}\Gamma_{\lambda f}^{1/2}}{E_\lambda - E}\,, \tag{2.8}$$

where $K_{nf}^{(0)}$ and $\Gamma_{\lambda f}^{1/2}$ are real quantities. We note that in general K_{nn} also has complex poles, so that Eq. (2.7) represents a plausible model rather than a general form.

2.2. *Scattering Matrix*

In the spirit of the work of Humblet and Rosenfeld [14], we write

$$S_{nn} = S_{nn}^{(0)} - i\sum_\lambda \frac{\omega_{\lambda n}}{E - e_\lambda + \frac{1}{2}i\omega_\lambda}\,, \tag{2.9}$$

$$S_{nf} = S_{nf}^{(0)} - i\sum_\lambda \frac{\omega_{\lambda n}^{1/2}\omega_{\lambda f}^{1/2}}{E - e_\lambda + \frac{1}{2}i\omega_\lambda}\,. \tag{2.10}$$

The complex resonance parameters appearing in these equations are not independent of one another because of the unitarity property of $\mathbf{S}$. This drawback is partly compensated by the fact that the poles of $\mathbf{S}$ are closely associated with metastable states [4].

2.3. *Model Background Phase Shift*

In the R-matrix [4, 15], Feshbach's [6], and the shell-model [5] approaches, one writes

$$\mathbf{S} = \exp(i\boldsymbol{\theta})(\mathbf{1} + i\tilde{\mathbf{K}})(\mathbf{1} - i\tilde{\mathbf{K}})^{-1} \exp(i\boldsymbol{\theta}), \tag{2.11}$$

where $\exp(2i\boldsymbol{\theta})$ is some (usually diagonal) background scattering matrix and $\tilde{\mathbf{K}}$ is the associated "model" reactance matrix. In the present one-particle channel case, Eq. (2.11) becomes

$$S_{nn} = \exp(2i\theta)\,\frac{1 + i\tilde{K}_{nn}}{1 - i\tilde{K}_{nn}}\,, \tag{2.12}$$

$$S_{nf} = 2i\exp(i\theta)\,\frac{\tilde{K}_{nf}}{1 - i\tilde{K}_{nn}}\,. \tag{2.13}$$

Here,

$$\tilde{K}_{nn} = \frac{K_{nn} - \tan\theta}{1 + K_{nn}\tan\theta}, \qquad \tilde{K}_{nf} = K_{nf}[\cos\theta + K_{nn}\sin\theta]^{-1} \tag{2.14}$$

are real quantities that can be parametrized as follows (see Eqs. (2.7) and (2.8)):

$$\tilde{K}_{nn} = \tilde{K}_{nn}^{(0)} + \frac{1}{2}\sum_{\lambda}\frac{\tilde{\Gamma}_{\lambda n}}{E_\lambda - E}, \tag{2.15}$$

$$\tilde{K}_{nf} = \tilde{K}_{nf}^{(0)} + \frac{1}{2}\sum_{\lambda}\frac{\tilde{\Gamma}_{\lambda n}^{1/2}\tilde{\Gamma}_{\lambda f}^{1/2}}{E_\lambda - E}. \tag{2.16}$$

In general, there exists no simple relationship between the resonance parameters of Eqs. (2.7) and (2.8) on the one hand and of Eqs. (2.15) and (2.16) on the other. However, in Section 2.5, we give such a relationship in the important case of the one-level approximation.

The practical usefulness of the introduction of a background phase shift θ derives from the fact that it can be chosen for instance, in such a way that

$$S_{nn}^{(0)} = \exp(2i\theta). \tag{2.17}$$

In [11, 16], the following parametrizations were used

$$S_{nn} = \exp(2i\theta)\left[\tilde{S}_{nn}^{(0)} - i\sum_{\lambda}\frac{\tilde{\omega}_{\lambda n}}{E - e_\lambda + \frac{1}{2}i\omega_\lambda}\right], \tag{2.18}$$

$$S_{nf} = \exp(i\theta)\left[S_{nf}^{(0)} - i\sum_{\lambda}\frac{\tilde{\omega}_{\lambda n}^{1/2}\tilde{\omega}_{\lambda f}^{1/2}}{E - e_\lambda + \frac{1}{2}i\omega_\lambda}\right], \tag{2.19}$$

with

$$\tilde{\omega}_{\lambda f} = \omega_{\lambda f}, \qquad \tilde{\omega}_{\lambda n}^{1/2} = \exp(-i\theta)\,\omega_{\lambda n}^{1/2}. \tag{2.20}$$

2.4. *Correlations and Average S-Matrix*

The average S-matrix in an energy interval of size I centered on E is given by [15]:

$$\langle \mathbf{S}\rangle = \langle \mathbf{S}(E + iI)\rangle. \tag{2.21}$$

We write

$$\mathbf{S} = \mathbf{S}^R + i\mathbf{S}^I, \qquad \langle\mathbf{S}\rangle = \langle\mathbf{S}^R\rangle + i\langle\mathbf{S}^I\rangle; \tag{2.22}$$

we use similar notations for $\mathbf{K}$ and $\langle\mathbf{K}\rangle$. From Eq. (2.11) (with $\theta = 0$), we find

$$\langle\mathbf{K}^R\rangle = \frac{2(1 + \langle\mathbf{S}^R\rangle)^{-1}\langle\mathbf{S}^I\rangle}{1 + \langle\mathbf{S}^R\rangle + \langle\mathbf{S}^I\rangle(1 + \langle\mathbf{S}^R\rangle)^{-1}\langle\mathbf{S}^I\rangle}, \tag{2.23}$$

$$\langle\mathbf{K}^I\rangle = \frac{2}{1 + \langle\mathbf{S}^R\rangle + \langle\mathbf{S}^I\rangle(1 + \langle\mathbf{S}^R\rangle)^{-1}\langle\mathbf{S}^I\rangle} - 1. \tag{2.24}$$

The usual assumption of a locally uniform distribution for the partial width amplitudes yields

$$\langle K^I\rangle_{cc'} = \tfrac{1}{2}(\pi/D)\langle \Gamma_{\lambda c}^{1/2}\Gamma_{\lambda c'}^{1/2}\rangle_\lambda, \tag{2.25}$$

where D is the average distance between adjacent levels, and $\langle\,\rangle_\lambda$ denotes an ensemble average. Hence, Eq. (2.24) relates the average S-matrix to the correlations between partial width amplitudes. The existence of such a relation was emphasized by Lane [17]. We may conclude that the problems of finding a dynamical description of the correlations and of deriving the expression of the average S-matrix are largely equivalent. In [15, 18–20], for instance, the DWBA was "derived" from a model for the correlation between the partial width amplitudes; the same attitude was adopted in [2–4] in the case of radiative capture. Conversely, an expression for the correlations has been derived from the DWBA in [12] in the case of radiative capture. In the latter case, Eq. (2.24) yields

$$\langle K_{nf}^I\rangle = -\frac{\langle S_{nn}^I\rangle\langle S_{nf}^I\rangle + \langle S_{nf}^R\rangle(1 + \langle S_{nn}^R\rangle)}{(\langle S_{nn}^I\rangle)^2 + (1 + \langle S_{nn}^R\rangle)^2}. \tag{2.26}$$

Similar relations may be written easily in the case of the tilded quantities of Section 2.2. We find, for instance,

$$\begin{aligned}\langle \tilde{K}_{nf}^I\rangle = {} & [-\cos\theta\{\langle S_{nf}^R\rangle(\langle S_{nn}^R\rangle + \cos 2\theta) + \langle S_{nf}^I\rangle(\langle S_{nn}^I\rangle + \sin 2\theta)\} \\ & + \sin\theta\{-\langle S_{nf}^R\rangle(\langle S_{nn}^I\rangle + \sin 2\theta) + \langle S_{nf}^I\rangle(\langle S_{nn}^R\rangle + \cos 2\theta)\}] \\ & \times [(\langle S_{nn}^R\rangle + \cos 2\theta)^2 + (\langle S_{nn}^I\rangle + \sin 2\theta)^2]^{-1}.\end{aligned} \tag{2.27}$$

Although this expression appears to be more complicated than (2.26), it may yield a simpler result in certain cases. For instance, most doorway state models [13] lead to a Lorentzian distribution for the average of the partial widths $\tilde{\Gamma}_{\lambda n}$, i.e., for $\langle\tilde{K}_{nn}^I\rangle$, while the distribution of the average of the quantities $\Gamma_{\lambda n}$ is less simple.

2.5. *One-Level Approximations*

We write Eqs. (2.7) and (2.8) in the form

$$K_{nn} = K_{nn}^{(\infty)} + \frac{1}{2}\frac{\Gamma_{\lambda n}}{E_\lambda - E}. \tag{2.28}$$

$$K_{nf} = K_{nf}^{(\infty)} + \frac{1}{2}\frac{\Gamma_{\lambda n}^{1/2}\Gamma_{\lambda f}^{1/2}}{E_\lambda - E}. \tag{2.29}$$

We assume that the quantities $K_{nn}^{(\infty)}$ and $K_{nf}^{(\infty)}$ are independent of energy in the energy region of interest and introduce similar assumptions for the tilded quantities of Section 2.2. We find the relations

$$K_{nn}^{(\infty)} = \frac{\tilde{K}_{nn}^{(\infty)} + \tan\theta}{1 - \tan\theta \tilde{K}_{nn}^{(\infty)}}, \tag{2.30}$$

$$\tilde{E}_\lambda = E_\lambda + \frac{1}{2}\frac{\tan\theta \tilde{\Gamma}_{\lambda n}}{1 - \tan\theta \tilde{K}_{nn}^{(\infty)}}, \tag{2.31}$$

$$\tilde{\Gamma}_{\lambda n}^{1/2}/\Gamma_{\lambda n}^{1/2} = \cos\theta - \sin\theta \tilde{K}_{nn}^{(\infty)} = (\cos\theta + \sin\theta K_{nn}^{(\infty)})^{-1}, \tag{2.32}$$

$$\tilde{K}_{nf}^{(\infty)} = \frac{K_{nf}^{(\infty)}}{\cos\theta + \sin\theta K_{nn}^{(\infty)}}, \tag{2.33}$$

$$\tilde{\Gamma}_{\lambda f}^{1/2} = \Gamma_{\lambda f}^{1/2} - \sin\theta \Gamma_{\lambda n}^{1/2} \tilde{K}_{nf}^{(\infty)}. \tag{2.34}$$

From Eqs. (2.32) and (2.34), we obtain

$$\tilde{\Gamma}_{\lambda f}^{1/2}\tilde{\Gamma}_{\lambda n}^{1/2} = (\Gamma_{\lambda f}^{1/2}\Gamma_{\lambda n}^{1/2} - \sin\theta \Gamma_{\lambda n} \tilde{K}_{nf}^{(\infty)})(\cos\theta - \sin\theta \tilde{K}_{nn}^{(\infty)}). \tag{2.35}$$

This result shows that the correlation between the tilded partial width amplitudes $\tilde{\Gamma}_{\lambda c}^{1/2}$ differs from that between the $\Gamma_{\lambda c}^{1/2}$ values. In particular, the tilded partial widths generally are correlated if the $\Gamma_{\lambda c}^{1/2}$ are uncorrelated and conversely (provided that $\tilde{K}_{nf}^{(\infty)} \neq 0$). Correspondingly, Eq. (2.34) shows that $\tilde{\Gamma}_{\lambda f}$ does not vanish when $\Gamma_{\lambda f} = 0$. In the latter case, Eqs. (2.32) and (2.34) yield

$$\tilde{\Gamma}_{\lambda f}^{1/2} = \frac{\tilde{K}_{nf}^{(\infty)} \tan\theta}{\tilde{K}_{nn}^{(\infty)} \tan\theta - 1} \tilde{\Gamma}_{\lambda n}^{1/2};$$

the radiative capture cross section then vanishes at $E = E_\lambda$ (see Eqs. (2.6)–(2.8)). Examples of physical situations where this can occur are given in [21–23].

We now discuss the connection between the correlations as discussed in Section 2.4 on the one hand, and Eq. (2.35) on the other. From Eq. (2.14), we obtain, with the notation of Section 2.4,

$$\langle \tilde{K}_{nf}^{I} \rangle = \{\langle K_{nf}^{I} \rangle (\cos\theta + \langle K_{nn}^{R} \rangle \sin\theta) - \langle K_{nn}^{I} \rangle \sin\theta \langle K_{nf}^{R} \rangle\}$$
$$\times \{(\cos\theta + \langle K_{nn}^{R} \rangle \sin\theta)^2 + (\langle K_{nn}^{I} \rangle \sin\theta)^2\}^{-1}. \tag{2.36}$$

If we follow Lane and Mughabghab [12] and make the identifications

$$\langle K_{nn}^{R} \rangle = K_{nn}^{(\infty)}, \qquad \langle K_{nf}^{R} \rangle = K_{nf}^{(\infty)}, \tag{2.37a}$$

we obtain from Eq. (2.36) a relation that differs from Eq. (2.35) by the presence of the term $\langle K_{nn}^{I} \rangle^2 \sin^2\theta$ in the last braces in Eq. (2.36). A related difference exists

between Eq. (2.33) and the one that gives $\langle \tilde{K}_{nf}^{R} \rangle$ (Section 2.4 and Eq. (2.36)). These differences show that the identifications $\langle K_{cc'}^{R} \rangle = K_{cc'}^{(\infty)}$ on the one hand and

$$\langle \tilde{K}_{nn}^{R} \rangle = \tilde{K}_{nn}^{(\infty)}, \qquad \langle \tilde{K}_{nf}^{R} \rangle = \tilde{K}_{nf}^{(\infty)}, \tag{2.37b}$$

on the other hand, are not equivalent (see Section 2.7). In practice, however, the meaningful values of θ are small; the two sets of assumptions are then almost identical.

We now turn to the S-matrix parametrizations, (2.9) and (2.10). From Eqs. (2.5) and (2.6), we find, with obvious notations,

$$S_{nn}^{(\infty)} = \frac{1 + iK_{nn}^{(\infty)}}{1 - iK_{nn}^{(\infty)}}, \qquad S_{nf}^{(\infty)} = 2i\frac{K_{nf}^{(\infty)}}{1 - iK_{nn}^{(\infty)}}, \tag{2.38}$$

$$\omega_\lambda^{1/2} = \Gamma_{\lambda n}^{1/2}[1 + (K_{nn}^{(\infty)})^2]^{-1/2}, \qquad \omega_{\lambda n}^{1/2} = \Gamma_{\lambda n}^{1/2}[1 - iK_{nn}^{(\infty)}]^{-1}, \tag{2.39}$$

$$e_\lambda = E_\lambda + \frac{1}{2}\frac{K_{nn}^{(\infty)}\Gamma_{\lambda n}}{1 + (K_{nn}^{(\infty)})^2}, \tag{2.40}$$

$$\omega_{\lambda f}^{1/2} = \Gamma_{\lambda f}^{1/2} + i\omega_{\lambda n}^{1/2} K_{nf}^{(\infty)} = \Gamma_{\lambda f}^{1/2} + \frac{1}{2}\Gamma_{\lambda n}^{1/2} S_{nf}^{(\infty)}. \tag{2.41}$$

We give the parametrization, (2.18)–(2.20), only in the special case (see Eq. (2.17)) $S_{nn}^{(\infty)} = \exp(2i\theta)$. Then, we have

$$S_{nn} = \exp(2i\theta)\left[1 - i\frac{\omega_\lambda}{E - e_\lambda + \frac{1}{2}i\omega_\lambda}\right], \tag{2.42}$$

$$S_{nf} = \exp(i\theta)\left[\tilde{S}_{nf}^{(\infty)} - i\frac{\omega_\lambda^{1/2}\omega_{\lambda f}^{1/2}}{E - e_\lambda + \frac{1}{2}i\omega_\lambda}\right], \tag{2.43}$$

$$\tilde{S}_{nf}^{(\infty)} = 2K_{nf}^{(\infty)}[1 + (K_{nn}^{(\infty)})^2]^{-1/2}, \qquad \tilde{\Gamma}_{\lambda n} = \omega_\lambda = \tilde{\omega}_{\lambda n}. \tag{2.44}$$

If $\Gamma_{\lambda f}^{1/2}$ and $\Gamma_{\lambda n}^{1/2}$ are not correlated, Eq. (2.41) shows that $\omega_{\lambda f}^{1/2}$ and $\omega_{\lambda n}^{1/2}$ are correlated. In particular, we have

$$\mathrm{Im}\ \omega_{\lambda f}^{1/2} = [\mathrm{Re}\ \omega_{\lambda n}^{1/2}]\, K_{nf}^{(\infty)} = \Gamma_{\lambda n}^{1/2}\frac{K_{nf}^{(\infty)}}{1 + (K_{nn}^{(\infty)})^2}. \tag{2.45}$$

A relation equivalent to (2.45) was derived in [11] in the frame of the shell-model approach. Our derivation shows that this relation is a direct consequence of the unitarity of S, so that the "correlation" between Im $\omega_{\lambda f}^{1/2}$ and $\Gamma_{\lambda n}^{1/2}$, as expressed by Eq. (2.45), can be considered as somewhat trivial. However, it may have some bearing with phenomenological correlations, as we discuss in the next section.

2.6. *Analysis of Experimental Data*

The formulas derived in the preceding sections illustrate the importance of Feshbach's warning [13] recalled in the introduction: The statistical properties of the resonance parameters depend on their detailed definition. The results of Sections 2.1–2.5 enable us to relate the correlation properties in different parametrizations.

In general, the neutron elastic scattering data are analyzed with the help of Eq. (2.42). The phenomenological neutron partial width can then be identified with $\omega_\lambda = \tilde{\Gamma}_{\lambda n}$ for the particular choice

$$\theta = \tan^{-1} K_{nn}^{(\infty)} . \tag{2.46}$$

which corresponds to $\tilde{K}_{nn}^{(\infty)} = 0$. Thus, the theoretical neutron partial width is equal to the phenomenological one only if the model potential scattering phase shift is equal to the observed background phase shift. This establishes a condition for the choice of the interaction radius in R-matrix theory, or of the choice of average potential well in the shell-model approach. We return to this point in Sections 3 and 4.

The value of the phenomenological photon width is usually obtained from the value of the area $\mathscr{A}$ under the resonance peak, after subtraction of the background. If we neglect the contribution of the skew-symmetric term to the area in $| S_{nf} |^2$, we obtain, from Eq. (2.43),

$$\begin{aligned} \mathscr{A} &\propto | \omega_{\lambda f} | - \omega_\lambda^{1/2} \operatorname{Im} \omega_{\lambda f}^{1/2} \tilde{S}_{nf}^{(\infty)} \\ &= | \omega_{\lambda f} | - \tfrac{1}{2} (\tilde{S}_{nf}^{(\infty)})^2 \omega_\lambda . \end{aligned} \tag{2.47}$$

In first order in the background, we find

$$\mathscr{A} = | \omega_{\lambda f} | \simeq \Gamma_{\lambda f} - 2 \frac{\Gamma_{\lambda n}^{1/2} \Gamma_{\lambda f}^{1/2} K_{nn}^{(\infty)} K_{nf}^{(\infty)}}{1 + (K_{nn}^{(\infty)})^2} . \tag{2.48}$$

For the choice (2.46) of the background phase shift θ, Eqs. (2.32) and (2.34) show that, in first order in $K_{nf}^{(\infty)}$,

$$| \omega_{\lambda f} | = \tilde{\Gamma}_{\lambda f} = \Gamma_{\lambda f} - \Gamma_{\lambda n}^{1/2} \Gamma_{\lambda f}^{1/2} \sin 2\theta K_{nf}^{(\infty)} . \tag{2.49}$$

From Eqs. (2.47)–(2.49), we see that the phenomenological photon width is closer to $| \omega_{\lambda f} | = \tilde{\Gamma}_{\lambda f}$ than to $\Gamma_{\lambda f}$.

2.7. *Discussion*

In Sections 2.1–2.3, we considered various parametric forms for the elastic and radiative capture cross sections. The parametrizations given in Sections 2.1 and 2.2 involve the poles and residues of the reactance and scattering matrices, respectively. In this sense, they are "model independent." In practice, however, it is often of interest to analyze the data with some prejudice concerning the description of the background, particularly in the elastic scattering channel. This corresponds to the introduction, a priori, of a model scattering phase shift θ and gives rise to the parametric forms studied in Section 2.3.

In the case of an isolated level, the resonance parameters of the various parametrizations can be related to each other (Section 2.5). Then, it is found that the correlation properties (for instance) of the partial widths depend on the parametrization that has been adopted, in particular, on the choice of θ. This was emphasized by Feshbach [13] in the general case. The problem of the "best choice" for θ may appear to be nonexistent if one takes into account the relationship between the resonance parameters (Section 2.5). In practice, however, it is convenient to choose θ in such a way that it leads to the standard way of analyzing the experimental data (Sections 2.5 and 2.6), although this is not necessary as far as the photon widths are concerned (see Sections 4.3 and 4.5). We discuss below that this choice of θ may be more delicate for the background cross section.

In Section 2.4, we showed that there exists a direct connection between the correlation of the partial widths and the average of the S-matrix (Eqs. (2.24) and (2.25)). Furthermore, Eq. (2.23) gives the background cross section in terms of the average S-matrix provided that an assumption is made, namely Eq. (2.37a) or Eq. (2.37b). These assumptions are much more model dependent than Eq. (2.25), because they essentially amount to an assumption that the background cross section underlying one isolated level arises from the "far-away" levels only [4]. If the model phase shift θ varies rapidly with energy, Eqs. (2.32) and (2.34) show that the corresponding mean partial widths also may be very dependent on energy; then, assumption (2.37b) may be quite inaccurate. This will be illustrated in Sections 4.4 and 4.5. By the same token, one realizes why assumptions (2.37a) and (2.37b) are not compatible for large θ.

3. Valence Capture Model

In the present section, we deal with the dynamical interpretation of the resonance parameters introduced in Section 2; in other words, we discuss their identification with quantities derived from a nuclear model. In Section 3.1, we give expressions for the elastic and capture cross sections in the frame of the shell-model approach. These expressions differ from those presented in [8, 11, 16] in two main respects: (i) We are chiefly concerned here with the reactance matrix representation, which presents several advantages over the S-matrix parametrization; it involves fewer parameters, embodies unitarity, is similar to the R-matrix approach, and is close to the phenomenological parametrization; and (ii) we make use of the convenient projection operator formalism of [8, 24–26].

In Section 3.2, we briefly recall, for comparison, the main features of the R-matrix approach. In Section 3.3, we formulate a model equivalent to the valence capture model of Lane and Lynn [1–4, 12], in the shell-model approach. We show that a numerical approximation used in [11, 16] is inaccurate in the (quantitatively important) surface region, and we construct a more accurate approximation. We exhibit in Section 3.4 the close analogy between our results for the valence capture model and those derived earlier by Lane and Lynn [1–4] from the R-matrix approach. Finally, the relationship [3, 4, 12] between our expressions, which involve a real potential well and the optical-model quantities is discussed in Section 3.5.

3.1. *Shell-Model Approach*

Following Feshbach [24–26], we introduce the projection operators P and $Q = 1 - P$, with the understanding that we work within some truncated Hilbert space of functions. The operator P is defined in such a way as to contain at least (see below) all the channel states. For definiteness, we shall often use the shell-model representation [5]. We call H_0 the independent particle Hamiltonian, δ_c the corresponding potential scattering phase shift in channel c, and V the residual interaction. The index c refers generically to all channels; the entrance neutron channel is denoted by n. We call ϕ_j the normalized bound eigenstates of H_0 and $\chi_E{}^c$ its scattering eigenstates with the asymptotic behavior, for s-wave neutrons,

$$\chi_E{}^c \sim \left(\frac{2}{\pi\hbar v_c}\right)^{1/2} \sin(kr + \delta_c)\, \psi_c\,. \tag{3.1}$$

We take here

$$Q = \sum_{j=1}^{J} \phi_j\rangle\langle\phi_j\,; \qquad P = \sum_c \int dE\, \chi_E{}^c\rangle\langle\chi_E{}^c + \sum_{m\neq j} \mid \phi_m\rangle\langle\phi_m \mid. \tag{3.2}$$

Below, we shall see why it may be convenient to introduce some (in practice at most one) bound states ϕ_m in the P-space (see, however, Section 5.6). The full standing wave $\tilde{\Psi}_E$ is the solution of the Lippmann–Schwinger equation [5]:

$$\tilde{\Psi}_E = \chi_E + (E - H_0)^{-1}\, V\tilde{\Psi}_E\,. \tag{3.3}$$

It has the asymptotic behavior, in the neutron channel n,

$$\tilde{\Psi}_E \sim \left(\frac{2}{\pi\hbar v_n}\right)^{1/2} [\sin(kr + \delta_n) + \tilde{K}_{nn} \cos(kr + \delta_n)]\, \psi_t\,. \tag{3.4}$$

One finds [24–26]:

$$\begin{aligned}\tilde{\Psi}_E = {} & [1 + P(E - PHP)^{-1}\, PVP]\, \chi_E{}^n + [1 + P(E - PHP)^{-1}\, PHQ] \\ & [E - QHQ - QHP(E - PHP)^{-1}\, PHQ]^{-1}\, QHP[1 + P(E - PHP)^{-1} \\ & PVP]\, \chi_E{}^n.\end{aligned} \tag{3.5}$$

We introduce the effective interaction

$$\bar{V} = V + VP(E - PHP)^{-1}\, PV, \tag{3.6}$$

and assume for simplicity that n is the only open channel. We diagonalize the matrix contained inside the square brackets in Eq. (3.5), and thereby obtain the energy eigenvalue $\tilde{E}_\lambda$, the eigenstates ξ_λ and the partial width amplitudes

$$\tilde{\Gamma}^{1/2}_{\lambda n}(E) = (2\pi)^{1/2}\langle\xi_\lambda \mid \bar{V} \mid \chi_E{}^n\rangle. \tag{3.7}$$

All of these quantities are real. The scattering matrix can be written in the form (compare with Eq. (2.12))

$$S_{nn} = \exp(2i\delta_n)\, \frac{1 + i\tilde{K}_{nn}}{1 - i\tilde{K}_{nn}}\,, \tag{3.8}$$

with

$$\tilde{K}_{nn} = \tilde{K}^{(0)}_{nn} + \frac{1}{2} \sum_{\lambda=1}^{J} \frac{\tilde{\Gamma}_{\lambda n}}{\tilde{E}_\lambda - E}\,, \tag{3.9}$$

$$K^{(0)}_{nn} = -\pi\langle\chi_E{}^n \mid \bar{V} \mid \chi_E{}^n\rangle. \tag{3.10}$$

To display explicit formulas, we assume henceforth that $V_m{}^c = \langle\chi_E{}^c \mid V \mid \phi_m\rangle$ and $V^{cc'}_{EE'} = \langle\chi_E{}^c \mid V \mid \chi^{c'}_{E'}\rangle$ can be treated in first-order perturbation theory. This assumption can be lifted easily. We obtain, after a few manipulations

$$\begin{aligned}\tilde{\Psi}_E = {} & \chi_E{}^n + \sum_c \int dE'\, (E - E')^{-1}\, V^{nc}_{EE'}\chi^c_{E'} + \sum_m (E - E_m)^{-1}\, V_{m^c}\phi_m \\ & + \sum_{\lambda=1}^{J} \frac{(2\pi)^{-1/2}\, \tilde{\Gamma}^{1/2}_{\lambda n}}{E - \tilde{E}_\lambda} \\ & \times \left[\xi_\lambda + \sum_c \int dE'\, (E - E')^{-1}(2\pi)^{-1/2}\, \tilde{\Gamma}^{1/2}_{\lambda c}(E')\, \chi^c_{E'} + \sum_m \frac{\phi_m\rangle\langle\phi_m \mid \bar{V} \mid \xi_\lambda\rangle}{E - E_m}\right].\end{aligned} \tag{3.11}$$

The radiative capture amplitude is given by Eqs. (2.13) and (2.16), where θ is replaced by δ_n and where

$$\tilde{K}_{nf}^{(0)} = -\langle \Psi_f \mid d \mid \chi_E{}^n \rangle - \sum_c \int dE'\,(E-E')^{-1}\, V_{EE'}^{nc} \langle \Psi_f \mid d \mid \chi_{E'}^c \rangle - \sum_m (E-E_m)^{-1} \langle \Psi_f \mid d \mid \phi_m \rangle \langle \phi_m \mid V \mid \chi_E{}^n \rangle, \tag{3.12}$$

$$\tilde{\Gamma}_{\lambda f}^{1/2} = (2/\pi)^{1/2} \langle \Psi_f \mid d \mid \xi_\lambda \rangle + \pi^{-1} \sum_c \int dE'\,(E-E')^{-1}\, \tilde{\Gamma}_{\lambda c}^{1/2}(E') \times \langle \Psi_f \mid d \mid \chi_{E'}^c \rangle + (2/\pi)^{1/2} \sum_m (E-E_m)^{-1} \langle \phi_m \mid \bar{V} \mid \xi_\lambda \rangle \langle \Psi_f \mid d \mid \phi_m \rangle. \tag{3.13}$$

To obtain the S-matrix parametrization, on which the discussion in [11, 16] was based, one replaces E by $E + i\epsilon$ in Eq. (3.5). By diagonalizing the resulting matrix (in the brackets), one gets complex resonance energies $e_\lambda - \frac{1}{2} i\omega_\lambda$ and complex resonance states Ω_λ. The S-matrix is given by Eqs. (2.18) and (2.19) with θ replaced by δ_n and with

$$\tilde{\omega}_{\lambda n}^{1/2}(E) = (2\pi)^{1/2} \langle \chi_E{}^n \mid \bar{V} \mid \Omega_\lambda \rangle, \tag{3.14}$$

$$\tilde{S}_{nn}^{(0)} = 1 - 2i\pi \langle \chi_E{}^n \mid V \mid \chi_E{}^n \rangle, \tag{3.15}$$

$$\tilde{S}_{nf}^{(0)} = -2i \left[\langle \Psi_f \mid d \mid \chi_E{}^n \rangle + \sum_c \int dE'\,(E^+ - E')^{-1}\, V_{EE'}^{cc'} \langle \Psi_f \mid d \mid \chi_{E'}^c \rangle \right], \tag{3.16}$$

$$\tilde{\omega}_{\lambda f}^{1/2} = (2/\pi)^{1/2} \left[\langle \Psi_f \mid d \mid \Omega_\lambda \rangle + \sum_c \int dE'\,(E^+ - E')^{-1} (2\pi)^{-1/2}\, \tilde{\omega}_{\lambda n}^{1/2}(E') \times \langle \Psi_f \mid d \mid \chi_{E'}^c \rangle + \sum_m (E-E_m)^{-1} (2\pi)^{-1/2} \langle \Psi_f \mid d \mid \phi_m \rangle \langle \phi_m \mid V \mid \Omega_\lambda \rangle \right]. \tag{3.17}$$

Here, we have assumed that $E_m < E$. This is in keeping with the assumption that the energy dependence of $\tilde{\omega}_{\lambda n}(E)$ is weak and with our forthcoming choice of the states ϕ_m (Sections 3.3 and 5.6).

3.2. *R-Matrix Approach*

Let a denote the interaction radius [15] that separates the internal from the external region. In the case of only one (s-wave) neutron channel, the R-matrix expansion for the standing wave $\tilde{\Psi}_E$ (Eq. (3.4) with $\delta_n = -ka$) is given by [15, 23]:

$$\tilde{\Psi}_E = \left(\frac{2}{\pi\hbar v}\right)^{1/2} \left\{ \psi_t \left[\sin k(r-a) + \frac{1}{2} \cos k(r-a) \sum_\lambda \frac{\tilde{\Gamma}_{\lambda n}}{\tilde{E}_\lambda - E} \right]_{\rm ER} + \left[\left(\frac{\hbar^2 k}{4M}\right)^{1/2} \sum_\lambda \frac{\tilde{\Gamma}_{\lambda n}^{1/2}}{E - \tilde{E}_\lambda} X_\lambda \right]_{\rm IR} \right\}. \tag{3.18}$$

The lower indices ER and IR indicate that the corresponding expression differs from zero in the external and internal regions, respectively. We put a tilde on the R-matrix eigenvalues and partial width in order to exhibit later the close analogy between the R-matrix and shell-model expressions; we also changed the conventional sign of $\tilde{\Gamma}_{\lambda n}^{1/2}$, for the same reason.

The scattering matrix is given by Eqs. (2.12) and (2.13), with

$$\tilde{K}_{nn}^{(0)} = 0, \qquad \tilde{K}_{nf}^{(0)} = \langle \Psi_f \mid d \mid S_E \psi_t \rangle_{\rm ER}, \tag{3.19}$$

$$\tilde{\Gamma}_{\lambda f}^{1/2} = \tilde{\Gamma}_{\lambda f,\rm ER}^{1/2} + \tilde{\Gamma}_{\lambda f,\rm IR}^{1/2}, \tag{3.20}$$

$$\tilde{\Gamma}_{\lambda f,\rm ER}^{1/2} = -\tilde{\Gamma}_{\lambda n}^{1/2} \langle \Psi_f \mid d \mid C_E \psi_t \rangle_{\rm ER}, \qquad \tilde{\Gamma}_{\lambda f,\rm IR}^{1/2} = (2/\pi)^{1/2} \langle \Psi_f \mid d \mid X_\lambda \rangle_{\rm IR}. \tag{3.21}$$

Here, we have introduced the single-particle wavefunction

$$S_E = \left(\frac{2}{\pi\hbar v}\right)^{1/2} \sin k(r-a), \qquad C_E = \left(\frac{2}{\pi\hbar v}\right)^{1/2} \cos k(r-a). \tag{3.22}$$

3.3. *Valence Capture Model in the Shell-Model Approach*

In the valence capture model [1–4, 12], it is assumed that the radiative capture process is dominated by those configurations (in $\tilde{\Psi}_E$ and in Ψ_f) that correspond to the target in its ground state (ψ_t) coupled (in our example of s-wave capture) to a nucleon in a s-wave state (for $\tilde{\Psi}_E$) or in a p-wave bound state (for Ψ_f). For $\tilde{\Psi}_E$, these configurations are, in the shell-model approach, $\chi_{E'}^n$ (all E') plus, in practice, at most one bound state ϕ_m. For nuclei with mass number slightly larger than the peak of the 3s giant resonance, for instance, a weakly bound 3s-neutron orbital exists for a standard choice of v_0 (see Section 5.6) and should be treated on the same footing as the scattering configuration $\chi_{E'}^n$. We denote by ϕ_m this weakly bound 3s single-particle state, coupled to the target state ψ_t.

The expression of the radiative capture amplitude in the valence capture model is given by Eqs. (2.13), (2.16), (3.12), and (3.13), where only the contributions of ϕ_m and of $\chi_{E'}^n$ are retained. To obtain explicit formulas, we make use of the short-range nature of the residual interaction V. In the open neutron channel, the following expression holds, for $r > r'$ (see Section 5.5),

$$\int dE'\,(E-E')^{-1} \mid \chi_{E'}^n(r) \rangle \langle \chi_{E'}^n(r') \mid + (E-E_m)^{-1} \mid \phi_m(r) \rangle \langle \phi_m(r') \mid = -\pi C_E{}^n(r)\, \psi_t \rangle \langle \chi_E{}^n(r') \mid. \tag{3.23}$$

Here, we write explicitly only the radial coordinate (r or r') of the valence neutron. The function $C_E{}^n(r)$ is the single-particle distorted scattering state with the *asymptotic* behavior (compare with (3.1) and (3.22)),

$$C_E{}^n(r) \sim \left(\frac{2}{\pi\hbar v}\right)^{1/2} \cos(kr + \delta_n). \tag{3.24}$$

The usefulness of Eq. (3.23) stems from the short-range nature of V, which restricts the radial coordinate in Eqs. (3.12) and (3.13) to the internal region, for all matrix elements involving V. Because of the long-range nature of the electromagnetic interaction, the external region, in contrast, can provide the main [30] contribution to $\langle \Psi_f \mid d \mid \chi_{E'}^n \rangle$ (see Section 4). Eqs. (3.11)–(3.13) and (3.23) yield the following values for the contribution of the external region to the radiative capture parameters:

$$[\tilde{\Gamma}_{\lambda f}^{1/2}]_{\mathrm{ER}} = -\tilde{\Gamma}_{\lambda n}^{1/2} \langle \Psi_f \mid d \mid C_E{}^n \psi_t \rangle_{\mathrm{ER}}, \tag{3.25}$$

$$[\tilde{K}_{nf}^{(0)}]_{\mathrm{ER}} = -\langle \Psi_f \mid d \mid X_E{}^n \rangle_{\mathrm{ER}} + \pi V_{EE}^{nn} \langle \Psi_f \mid d \mid C_E{}^n \psi_t \rangle_{\mathrm{ER}}, \tag{3.26}$$

where ER indicates that the integration runs over the external region only.

To obtain the contribution of the internal region (IR), we use the factorization approximation [4],

$$(\chi_{E'})_{\mathrm{IR}} = f(E', E)(\chi_E)_{\mathrm{IR}}; \qquad f(E, E) = 1. \tag{3.27}$$

The accuracy of this approximation has been checked by several authors [27–29]. In [28, 29], it was applied to radiative capture in the region of the giant dipole resonance. There, the contribution of the ER is small and Eq. (3.27) can be used in all space without any significant loss of accuracy. This is not true for low-energy neutrons, particularly in the region of the peak in the s-wave neutron strength function. There, the ER dominates the radiative capture amplitude [30] (see Section 4). Then, approximation (3.27) must be confined strictly to the IR. This was not recognized in [16].

We use approximation (3.27) for the matrix elements of V and for the contribution of the IR to the matrix elements of d. This yields the following contribution of the internal region to $\tilde{K}_{nf}^{(0)}$ and $\tilde{\Gamma}_{\lambda f}^{1/2}$:

$$\begin{aligned}[\tilde{K}_{nf}^{(0)}]_{\mathrm{IR}} &= -\langle \Psi_f \mid d \mid X_E{}^n \rangle_{\mathrm{IR}} (1 + F V_{EE}^{nn}) - (E - E_m)^{-1} \\ &\quad \times \langle \Psi_f \mid d \mid \phi_m \rangle_{\mathrm{IR}} \langle \phi_m \mid V \mid \chi_E{}^n \rangle,\end{aligned} \tag{3.28}$$

$$\begin{aligned}[\tilde{\Gamma}_{\lambda f}^{1/2}]_{\mathrm{IR}} &= +\tilde{\Gamma}_{\lambda n}^{1/2} (F/\pi) \langle \Psi_f \mid d \mid \chi_E{}^n \rangle_{\mathrm{IR}} + (2/\pi)^{1/2} (E - E_m)^{-1} \\ &\quad \times \langle \phi_m \mid V \mid \xi_\lambda \rangle \langle \Psi_f \mid d \mid \phi_m \rangle_{\mathrm{IR}},\end{aligned} \tag{3.29}$$

where

$$F = \int dE' \, (E - E')^{-1} f^2(E', E). \tag{3.30}$$

Since ϕ_m is normalized to unity in all space, the last term on the right-hand side of Eq. (3.28) and of Eq. (3.29), respectively, remains finite when $(E - E_m) \to 0$. We return to this point in Section 5.6.

It is convenient, to introduce the following normalized single-particle states, where $s_f{}^2$ denotes the spectroscopic factor of the final state

$$t_f = s_f^{-1} \langle \psi_t \mid \Psi_f \rangle, \qquad t_E = t_E{}^n = \langle \psi_t \mid \chi_E{}^n \rangle, \qquad (t_m)_{\mathrm{IR}} = \langle \psi_t \mid \phi_m \rangle_{\mathrm{IR}},$$
$$w_E = (C_E{}^n)_{\mathrm{ER}} - (F/\pi)(t_E{}^n)_{\mathrm{IR}}. \tag{3.31}$$

Eqs. (3.25)–(3.29) take the form

$$\begin{aligned}\tilde{K}_{nf}^{(0)} &= -s_f [\langle t_f \mid d \mid t_E{}^n \rangle - \pi V_{EE}^{nn} \langle t_f \mid d \mid w_E \rangle] - (E - E_m)^{-1} \\ &\quad \times \langle t_f \mid d \mid t_m \rangle_{\mathrm{IR}} \langle \phi_m \mid V \mid \chi_E{}^n \rangle,\end{aligned} \tag{3.32}$$

$$\tilde{\Gamma}_{\lambda f}^{1/2} = -s_f \tilde{\Gamma}_{\lambda n}^{1/2} \langle t_f \mid d \mid w_E \rangle + (2/\pi)^{1/2} (E - E_m)^{-1} \langle \phi_m \mid \bar{V} \mid \xi_\lambda \rangle \langle t_f \mid d \mid t_m \rangle_{\mathrm{IR}}. \tag{3.33}$$

For simplicity, we kept the notation d for the dipole operator sandwiched between two single-particle states.

The expression for the parameters of the reactance matrix (see Eqs. (2.5)–(2.8), (2.28), (2.29)) can be obtained from Eqs. (2.30)–(2.34), in the frame of the one-level approximation. The quantity $\tilde{K}_{nf}^{(\infty)}$ appearing in Eq. (2.34) can be expressed in terms of $\tilde{K}_{nn}^{(\infty)}$ by means of Eqs. (3.32) and (3.33). For simplicity (see Section 5.5), we drop the last term on the right-hand side of these equations. Then, we find

$$\tilde{K}_{nf}^{(\infty)} = -s_f [\langle t_f \mid d \mid t_E{}^n \rangle + \tilde{K}_{nn}^{(\infty)} \langle t_f \mid d \mid w_E \rangle], \tag{3.34}$$

$$\Gamma_{\lambda f}^{1/2} = \Gamma_{\lambda n}^{1/2} s_f [-\langle t_f \mid d \mid w_E \rangle \cos \delta_n - \langle t_f \mid d \mid t_E \rangle \sin \delta_n]. \tag{3.35}$$

Note that the channel–channel coupling V_{EE}^{nn} does not appear in these relations. The background part $S_{nf}^{(\infty)}$ of S_{nf} is given by Eqs. (2.38) and (3.32)–(3.35). If the average potential v_0 is chosen in such a way that $\tilde{K}_{nn}^{(\infty)} = 0$, i.e., in such a way that the shell-model potential scattering phase shift δ_n is equal to the observed background phase shift, one finds

$$S_{nf}^{(\infty)} = 2ie^{i\delta_n} \langle t_f \mid d \mid t_E \rangle s_f. \tag{3.36}$$

In other words, the background cross section is then equal to the direct capture cross section, in the frame of the valence capture model.

Proceeding along the same lines, one can obtain the expression for the complex photon width $\tilde{\omega}_{\lambda f}$ (Eqs. (2.19), (2.20)), defined in terms of the residues of the S-matrix. One finds, when neglecting the contribution of ϕ_m in the internal region

$$\tilde{\omega}_{\lambda f}^{1/2} / \tilde{\omega}_{\lambda n}^{1/2} = s_f [-e^{i\delta_n} \langle t_f \mid d \mid h_E \rangle_{\mathrm{ER}} - i \langle t_f \mid d \mid t_E \rangle_{\mathrm{IR}}] + \frac{F}{\pi} \langle t_f \mid d \mid t_E \rangle_{\mathrm{IR}} \tag{3.38}$$

$$= s_f [-i \langle t_f \mid d \mid t_E \rangle - \langle t_f \mid d \mid w_E \rangle], \tag{3.39}$$

where h_E is the single-particle distorted wave with the asymptotic behavior

$$h_E(r) \sim \left(\frac{2}{\pi\hbar v}\right)^{1/2} \exp(ikr). \qquad (3.40)$$

Note that the imaginary part of the ratio $\tilde{\omega}_{\lambda f}^{1/2}/\tilde{\omega}_{\lambda n}^{1/2}$ is given by the first term on the right-hand side of Eq. (3.39), in which the integration runs over all space. The square of this quantity was plotted versus A in [16], for a specific choice of v_0. We return to the latter point in Section 4. The real part of expression (3.39) is identical to $\tilde{\Gamma}_{\lambda f}^{1/2}/\tilde{\Gamma}_{\lambda n}^{1/2}$ (see Eq. (3.33)).

3.4. *Valence Capture Model in R-Matrix Theory*

Equations (3.19) and (3.21) give the external region contributions to $\tilde{K}_{nf}^{(0)}$ and $\tilde{\Gamma}_{nf}^{1/2}$, respectively. The close analogy with relations (3.25) and (3.26) is apparent in the case $V_{EE}^{nn} = 0$, which corresponds to $\tilde{K}_{nn}^{(0)} = 0$. The main difference is that $C_E{}^n$ in Eqs. (3.25) and (3.26) is distorted by the average potential v_0, while the hard sphere value (3.22) appears in Eqs. (3.19) and (3.21). The contribution of the internal region to $\tilde{\Gamma}_{\lambda f}^{1/2}$ is given by Eq. (3.21). Its explicit form in the valence capture model requires a model (intermediate coupling model) for the spreading of a single-particle state (analogous to $\chi_E{}^n$) among the R-matrix eigenstates X_λ [2–4]. This leads to the introduction of optical-model wavefunctions.

3.5. *Relationship with Optical-Model Quantities*

In Section 2.4, we discussed in general terms the connection between the average S-matrix and the correlation between partial width amplitudes. In the case of radiative capture, this connection was first pointed out by Lane and Lynn [2–4], and a simple derivation has been given recently by Lane and Mughabghab [12]. These papers also deal with the background cross section. The main purpose of the present section is threefold. First, we extend the derivation of [12] to the model reactance matrix, i.e., to the (tilded) quantities introduced in Section 2.3; this is quite easy but will be useful later. Second, and most important, we derive, in the frame of the shell-model approach, expressions for the ratio of the photon partial width to the neutron width, and for the background cross section. Finally, we show that these expressions, which only involve a real potential well, are at least formally compatible with those derived by Lane, Lynn, and Mughabghab [2–4, 12], which involve a complex optical-model potential. The quantitative equivalence between the two approaches will be discussed in Section 4.

Henceforth, the index opt refers to optical-model quantities. We call u_{opt} the scattering wavefunction with the asymptotic behavior

$$u_{\text{opt}}(E) = \left(\frac{2}{\pi\hbar v}\right)^{1/2} (\sin kr + \tan \delta_{\text{opt}} \cos kr). \qquad (3.41)$$

Lane and Mughabghab [12] make the assumption that (Eq. (2.3))

$$u_{\text{opt}}(E) = u(E + iI). \qquad (3.42)$$

Then Eq. (2.6) yields (see Eq. (2.22))

$$\langle K_{nf}^I \rangle = -s_f \operatorname{Im}\langle t_f \mid d \mid u_{\text{opt}} \rangle. \qquad (3.43)$$

Since

$$\langle K_{nn}^I \rangle = \operatorname{Im} \tan \delta_{\text{opt}}, \qquad (3.44)$$

Eqs. (3.43) and (2.25) give

$$\frac{\langle \Gamma_{\lambda f}^{1/2} \Gamma_{\lambda n}^{1/2} \rangle}{\langle \Gamma_{\lambda n} \rangle} = -s_f \frac{\operatorname{Im}\langle t_f \mid d \mid u_{\text{opt}} \rangle}{\operatorname{Im} \tan \delta_{\text{opt}}}. \qquad (3.45)$$

A corresponding relation can be derived for the quantities $\tilde{\Gamma}_{\lambda c}^{1/2}$ appearing in the model reactance matrix (Section 2.3). We have, from Eqs. (2.14),

$$\langle \tilde{K}_{nf} \rangle = \frac{\langle K_{nf} \rangle \cos \delta_{\text{opt}}}{\cos(\delta_{\text{opt}} - \theta)}, \qquad (3.46)$$

$$\langle \tilde{K}_{nn} \rangle = \tan(\delta_{\text{opt}} - \theta), \qquad (3.47)$$

$$\frac{\langle \tilde{\Gamma}_{\lambda f}^{1/2} \tilde{\Gamma}_{\lambda n}^{1/2} \rangle}{\langle \tilde{\Gamma}_{\lambda n} \rangle} = -s_f \left\{ \operatorname{Im} \frac{\langle t_f \mid d \mid u_{\text{opt}} \rangle \cos \delta_{\text{opt}}}{\cos(\delta_{\text{opt}} - \theta)} \right\} [\operatorname{Im} \tan(\delta_{\text{opt}} - \theta)]^{-1}. \qquad (3.48)$$

Note that the derivation of these relations is based on two assumptions. First, the valence model was used when retaining only the entrance channel component of Ψ_{E+iI}. Second, Eq. (3.42) requires a specific choice among the family of optical-model potentials that reproduce the average value $\langle S_{nn} \rangle$ of the scattering matrix. Nevertheless, the derivation can be regarded as fairly general, in the sense that it does not explicitly involve any detailed microscopic description.

The shell-model expression (3.33) yields, when neglecting the contribution of ϕ_m to the internal region,

$$\tilde{\Gamma}_{\lambda f}^{1/2}/\tilde{\Gamma}_{\lambda n}^{1/2} = -s_f \langle t_f \mid d \mid w_E \rangle, \qquad (3.49)$$

$$\langle \tilde{\Gamma}_{\lambda f}^{1/2} \tilde{\Gamma}_{\lambda n}^{1/2} \rangle / \tilde{\Gamma}_{\lambda n} = -s_f \langle t_f \mid d \mid w_E \rangle. \qquad (3.50)$$

From Eq. (3.35), we obtain

$$\langle \Gamma_{\lambda f}^{1/2} \Gamma_{\lambda n}^{1/2} \rangle / \langle \Gamma_{\lambda n} \rangle = -s_f [\langle t_f \mid d \mid w_E \rangle \cos \delta_n + \langle t_f \mid d \mid t_E \rangle \sin \delta_n]. \qquad (3.51)$$

Eqs. (3.33) and (3.35) show that there exists a full correlation between $\tilde{\Gamma}_{\lambda f}^{1/2}$ and $\tilde{\Gamma}_{\lambda n}^{1/2}$, or between $\Gamma_{\lambda f}^{1/2}$ and $\Gamma_{\lambda n}^{1/2}$. This result is more specific than (3.48).

The relationship between Eqs. (3.45) and (3.51), or between Eqs. (3.48) and (3.50), becomes clear if we retain only the external region (ER) contribution to $\Gamma_{\lambda f}^{1/2}$ (or to $\tilde{\Gamma}_{\lambda f}^{1/2}$), and assume that one can use the asymptotic forms (3.1), (3.24), and (3.41). Then, we find the same result from Eqs. (3.45) on the one hand and from Eq. (3.51) on the other hand, namely

$$\langle [\Gamma_{\lambda f}^{1/2}]_{\mathrm{ER}}\, \Gamma_{\lambda n}^{1/2} \rangle / \langle \Gamma_{\lambda n} \rangle = -s_f \left(\frac{2}{\pi \hbar v}\right)^{1/2} \langle t_f \mid d \mid \cos kr \rangle_{\mathrm{ER}} . \tag{3.52}$$

From Eqs. (3.48) and (3.50), we obtain, under the same conditions

$$\langle [\tilde{\Gamma}_{\lambda f}^{1/2}]_{\mathrm{ER}}\, \tilde{\Gamma}_{\lambda n}^{1/2} \rangle / \langle \tilde{\Gamma}_{\lambda n} \rangle = -s_f \left(\frac{2}{\pi \hbar v}\right)^{1/2} \langle t_f \mid d \mid \cos(kr + \delta_n) \rangle_{\mathrm{ER}} . \tag{3.53}$$

If δ_n is replaced by the hard sphere scattering phase shift, Eq. (3.53) reduces to a formula first obtained by Lane and Lynn [2–4]. Eqs. (3.52) and (3.53) can also be obtained directly from Eqs. (2.3), (2.6), and (2.7) (see Section 5).

Finally, we turn to the background cross section. By definition, this requires the use of a one-level approximation. Lane and Mughabghab make the identification (see Eq. (2.37a)) $K_{nn}^{(\infty)} = \langle K_{nn}^R \rangle$. Then, Eqs. (2.38) yield the relation [12],

$$S_{nf}^{(\infty)} = -2is_f \frac{\mathrm{Re}\langle t_f \mid d \mid u_{\mathrm{opt}} \rangle}{1 - i \,\mathrm{Re} \tan \delta_{\mathrm{opt}}} . \tag{3.54}$$

Alternatively, one can tentatively use assumption (2.37b) (see, however, Section 4):

$$\tilde{K}_{nn}^{(\infty)} = \langle \tilde{K}_{nn}^R \rangle, \tag{3.55}$$

which yields

$$S_{nf}^{(\infty)} = -2ie^{i\theta} s_f \frac{\mathrm{Re}\{\langle t_f \mid d \mid u_{\mathrm{opt}} \cos \delta_{\mathrm{opt}} / \cos(\delta_{\mathrm{opt}} - \theta) \rangle\}}{1 - i \,\mathrm{Re} \tan(\delta_{\mathrm{opt}} - \theta)} . \tag{3.56}$$

The shell-model expressions can be derived from Eqs. (2.30), (2.33), and (3.34). If one uses assumption (2.37a), namely, $K_{nn}^{(\infty)} \simeq \langle K_{nn}^R \rangle = \mathrm{Re} \tan \delta_{\mathrm{opt}}$, one finds

$$\begin{aligned} S_{nf}^{(\infty)} = {} & -2is_f \{ \langle t_f \mid d \mid t_E \rangle (\cos \delta_n + \sin \delta_n \,\mathrm{Re} \tan \delta_{\mathrm{opt}}) \\ & - (\sin \delta_n - \cos \delta_n \,\mathrm{Re} \tan \delta_{\mathrm{opt}}) \langle t_f \mid d \mid w_E \rangle \} \{1 - i \,\mathrm{Re} \tan \delta_{\mathrm{opt}}\}^{-1} \end{aligned} \tag{3.57}$$

If one uses assumption (2.37b) instead, one obtains

$$\begin{aligned} S_{nf}^{(\infty)} = {} & -2is_f e^{i\delta_n} \{ \langle t_f \mid d \mid t_E \rangle + \langle t_f \mid d \mid w_E \rangle \,\mathrm{Re} \tan(\delta_{\mathrm{opt}} - \delta_n) \} \\ & \times \{1 - i \,\mathrm{Re} \tan(\delta_{\mathrm{opt}} - \delta_n)\}^{-1}. \end{aligned} \tag{3.58}$$

For a choice of v_0 such that

$$\mathrm{Re} \tan(\delta_{\mathrm{opt}} - \delta_n) = 0, \tag{3.59}$$

one retrieves Eq. (3.36): The background and direct cross sections are then equal. At very low energy, Eq. (3.59) is tantamount to choosing v_0 in such a way that it reproduces the experimental scattering length.

It is of interest to write down the contribution of the external region to $S_{nf}^{(\infty)}$. From Eq. (3.57), we obtain

$$\begin{aligned} [S_{nf}^{(\infty)}]_{\mathrm{ER}} = {} & -2is_f \left(\frac{2}{\pi \hbar v}\right)^{1/2} \{1 - i \,\mathrm{Re} \tan \delta_{\mathrm{opt}}\}^{-1} \langle t_f \mid d \mid \sin kr \\ & + \mathrm{Re} \tan \delta_{\mathrm{opt}} \cos kr \rangle_{\mathrm{ER}} ; \end{aligned} \tag{3.60}$$

Eq. (3.58) yields

$$\begin{aligned} [S_{nf}^{(\infty)}]_{\mathrm{ER}} = {} & -2is_f \left(\frac{2}{\pi \hbar v}\right)^{1/2} e^{i\delta_n} \{1 - i \,\mathrm{Re} \tan(\delta_{\mathrm{opt}} - \delta_n)\}^{-1} \\ & \times \langle t_f \mid d \mid \sin(kr + \delta_n) + \cos(kr + \delta_n) \,\mathrm{Re} \tan(\delta_{\mathrm{opt}} - \delta_n) \rangle_{\mathrm{ER}} . \end{aligned} \tag{3.61}$$

While expression (3.61) depends on the choice of v_0 (via δ_n), the value (3.60) does not. This reflects the dynamical difference between assumptions (2.37) and (3.55). Note that Eq. (3.54) yields the ER contribution (3.60), while Eq. (3.56) gives Eq. (3.61).

We have seen that the contributions of the ER to the expressions involving optical-model quantities are identical to those involving shell-model quantities. We now discuss the relationship between the two approaches in the internal region. From Eqs. (3.11) and (3.27), we find, in the internal region and when omitting the contribution of ϕ_m (which could be included easily by a slight modification of the definition of F),

$$[\tilde{u}_{E+iI}]_{\mathrm{IR}} = [t_E]_{\mathrm{IR}} \{1 - (F/\pi) \tan(\delta_{\mathrm{opt}} - \delta_n)\}. \tag{3.62}$$

We also have

$$\tilde{u}_{E+iI} = \frac{\cos \delta_{\mathrm{opt}}}{\cos(\delta_{\mathrm{opt}} - \delta_n)} u_{E+iI} . \tag{3.63}$$

If we assume that Eqs. (3.42) and (3.55) hold, we find

$$[u_{\mathrm{opt}}]_{\mathrm{IR}} = [t_E]_{\mathrm{IR}} \{\cos(\delta_{\mathrm{opt}} - \delta_n) - (F/\pi) \sin(\delta_{\mathrm{opt}} - \delta_n)\} \sec \delta_{\mathrm{opt}} . \tag{3.64}$$

Hence, we have

$$[\mathrm{Im}\, u_{\mathrm{opt}}]_{\mathrm{IR}} = [t_E]_{\mathrm{IR}}\,(\sin\delta_n - (F/\pi)\cos\delta_n)\,\mathrm{Im}\tan\delta_{\mathrm{opt}}\,, \tag{3.65}$$

$$[\mathrm{Re}\, u_{\mathrm{opt}}]_{\mathrm{IR}} = [t_E]_{\mathrm{IR}}\,\{\cos\delta_n + \sin\delta_n\,\mathrm{Re}\tan\delta_{\mathrm{opt}} + (F/\pi)[\sin\delta_n - \cos\delta_n\,\mathrm{Re}\tan\delta_{\mathrm{opt}}]\}. \tag{3.66}$$

Eqs. (3.31) and (3.65) show the equivalence between the IR contributions to expressions (3.45) and (3.51); Eq. (3.66) relates the IR contributions in expressions (3.54) and (3.57). Similarly, one can related the IR contributions in expressions (3.48) and (3.56), and (3.50) and (3.58).

Equation (3.65) and (3.66) shed some light on the implications and limitations of the dynamical approach. The ambition of the approach consists in using a real rather than a complex potential well, thereby reducing the number of parameters in the theory. This leads to the appearance of the quantity F. When v_0 is changed, all the quantities on the right-hand side of Eqs. (3.65) and (3.66) vary. Hence, it is likely that the latter relations hold only for a specific choice of v_0. This appears natural (see Section 2.7), since they rely on assumption (3.55). However, it must be kept in mind that even the expressions that do not involve v_0, like (3.54) for instance, rely on a rather stringent assumption, namely relation (3.42), which need not be true in the internal region for the phenomenological optical-model potential. Note that relations (3.65) and (3.66) imply that Re u_{opt} and Im u_{opt} should have the same zeros in the IR. This is not the case for local optical-model potentials, but may well hold true for nonlocal ones.

3.6. *Discussion*

In the preceding sections, we derived various expressions for the photon width and for the background cross section, in the frame of the shell-model formulation of valence radiative capture; we also showed that our results are consistent with those of Lane, Lynn, and Mughabghab [1–4, 12]. Section 3.1 contains general shell-model expressions, which are specialized to the valence capture model in Section 3.3. We consider the various possible parametrizations described in Section 2. The comparison between our results for the contribution of the external capture to the photon width with that obtained from R-matrix theory (Section 3.2) shows that a close similarity exists between the two approaches (see Section 5.2). To compare the contributions of internal capture to the photon width in both approaches, one must relate the shell-model expressions, which involve a real potential well to optical-model quantities, since the latter appear in the results of [1–4, 12]. We show that the results obtained from these two choices for the average potential well are at least compatible with each other. We will see in Sections 4.3 and 4.5 that this formal consistency between apparently different expressions for the photon widths is also numerically very accurate.

The derivation of explicit expressions for the background capture cross section $\sigma_{nf}^{\mathrm{BG}}$ requires, in all approaches, the use of at least one additional dynamical assumption, namely (2.37a) or (2.37b). We recall (see Sections 2.4 and 2.7) that these two assumptions differ in the case when the model potential phase shift is large. In Section 3.5, we derive the expression for the background cross sections from assumptions (2.37a) or (2.37b), in the frame of the shell-model and of the Lane–Mughabghab approach. Thus, we obtain two couples of expressions, one that corresponds to assumption (2.37a) (Eqs. (3.54) and (3.57)), and another that is derived from assumption (2.37b) (Eqs. (3.56) and (3.58)). We will see in Sections 4.4 and 4.5c that the shell-model and optical-model expressions are numerically completely equivalent, but that they depend on the use of assumption (2.37a) or (2.37b), as expected from the discussion in Section 2.7.

4. Numerical Results

4.1. *Introduction*

In this section, we present numerical results on the valence capture model, in the vicinity of the 3s-peak in the neutron strength function, i.e., for mass number A close to 60. Our purpose is manifold. (1) In Section 4.2, we discuss the best choice for the single-particle potential well in the shell-model approach. We will see that this is an important, delicate, and instructive topic. (2) We compare the numerical values obtained from the two main approaches described in the previous sections, namely, that of Lane, Lynn, and Mughabghab [1–4, 12], which involves optical-model quantities, and the shell-model approach, which uses a real average potential well. (3) In Section 4.3, we study the dependence on mass number of the photon width $\Gamma_{\lambda f}$ and of the ratio $\Gamma_{\lambda f}/\Gamma_{\lambda n}$ of the photon and neutron widths, for thermal energy and for $E = 100$ keV, respectively. We also compare several definitions of the partial widths, i.e., definitions in terms of the residues appearing in the reactance matrix $\mathbf{K}$ (Section 2.a), in the "model" reactance matrix $\tilde{\mathbf{K}}$ (Section 2.3) and in the "model" scattering matrix $\mathbf{S}$ (Eq. (2.19)), respectively. This also illustrates Feshbach's remark reproduced in Section 1. We study the sensitivity of the results on the choice of the (real or complex) single-particle potential. (4) In Section 4.4, we investigate the dependence on mass number of the background cross section σ^{BG}, at thermal energy and (mainly) at $E = 100$ keV, respectively. We use several expressions and single-particle potentials. (5) In Section 4.5, we discuss the dependence on energy of the σ^{BG} and of the partial widths, for $A = 60$. Here again, we compare the results of several approximations and single-particle potentials. (6) Section 4.6 is devoted to the comparison between theoretical and experimental values in the cases ^{56}Fe(n, γ) and ^{60}Ni(n, γ).

It is convenient to summarize here and to simplify somewhat our main previous results. Since in the valence capture model $\Gamma_{\lambda f}^{1/2}$ and $\Gamma_{\lambda n}^{1/2}$ are proportional to each other, we write

$$\Gamma_{\lambda f}/\Gamma_{\lambda n} = (\langle \Gamma_{\lambda f}^{1/2}\Gamma_{\lambda n}^{1/2}\rangle/\langle \Gamma_{\lambda n}\rangle)^2 = \langle \Gamma_{\lambda f}\rangle/\langle \Gamma_{\lambda n}\rangle, \tag{4.1}$$

$$\pi\Gamma_{\lambda f}/D = 2(\text{Im} \tan \delta_{\text{opt}})(\Gamma_{\lambda f}/\Gamma_{\lambda n}). \tag{4.2}$$

The dipole operator contains trivial kinematical factors that can be factorized. In the case of the $s \to p$ single-particle transition, we write thus

$$\frac{\Gamma_{\lambda f}}{\Gamma_{\lambda n}} = \left\{\frac{4\pi}{9}\frac{e^2}{(\hbar c)^3} s_f{}^2 E_\gamma{}^3 \frac{Z^2}{A^2}\right\} | J |^2, \tag{4.3}$$

$$\sigma^{\text{BG}} = \left\{\frac{16\pi^2}{9}\frac{e^2}{(\hbar c)^3} k_n^{-2} s_f{}^2 E_\gamma{}^3 \frac{Z^2}{A^2}\right\} | I |^2, \tag{4.4}$$

where in the matrix elements I and J the operator d is replaced by the radial distance r (see Eqs. (4.5)–(4.12) below); E_γ denotes the photon energy. Henceforth, we set the spectroscopic factor $s_f{}^2$ equal to unity, except in Section 4.6, where we compare theory with experiment.

Equations (3.45) and (3.48) yield J and I in terms of optical-model quantities: With obvious notation, we have

$$J = \text{Im} \langle t_f \mid r \mid u_{\text{opt}}\rangle/\text{Im} \tan \delta_{\text{opt}}\,, \tag{4.5}$$

$$\tilde{J} = [\text{Im} \langle t_f \mid r \mid u_{\text{opt}}\rangle \cos \delta_{\text{opt}}/\cos(\delta_{\text{opt}} - \delta_n)][\text{Im} \tan(\delta_{\text{opt}} - \delta_n)]^{-1}, \tag{4.6}$$

where the normalization of u_{opt} is specified in Eq. (3.41), while δ_n is the model potential scattering phase shift. In the shell-model approach, we have (see Eqs. (3.50) and (3.51)):

$$J = \langle t_f \mid r \mid w_E\rangle \cos \delta_n + \langle t_f \mid r \mid t_E\rangle \sin \delta_n\,, \tag{4.7}$$

$$\tilde{J} = \langle t_f \mid r \mid w_E\rangle\,, \tag{4.8}$$

where w_E and t_E are given by Eqs. (3.1), (3.24), and (3.31). By analogy with R-matrix theory, we call a the radius of the internal region (IR) introduced in the factorization approximation (3.27).

The value of I in terms of optical-model quantities is given by Eqs. (3.54) or (3.56), depending on the basic assumption that is made (see Eqs. (2.37a) and (2.37b))

$$I = [\text{Re} \langle t_f \mid r \mid u_{\text{opt}}\rangle][1 - i \,\text{Re} \tan \delta_{\text{opt}}]^{-1}, \tag{4.9}$$

$$I = \{\text{Re} [\langle t_f \mid r \mid u_{\text{opt}}\rangle \cos \delta_{\text{opt}}/\cos(\delta_{\text{opt}} - \delta_n)]\}\{1 - i \,\text{Re} \tan(\delta_{\text{opt}} - \delta_n)\}^{-1}. \tag{4.10}$$

Eqs. (3.57) (based on Eq. (2.37a)) and (3.58) (based on Eq. (2.37b)) lead to the following shell-model expressions, respectively

$$I = \{\langle t_f \mid r \mid t_E\rangle(\cos \delta_n + \sin \delta_n \,\text{Re} \tan \delta_{\text{opt}}) - (\sin \delta_n - \cos \delta_n \,\text{Re} \tan \delta_{\text{opt}})\langle t_f \mid r \mid w_E\rangle\}\{1 - i \,\text{Re} \tan \delta_{\text{opt}}\}^{-1}, \tag{4.11}$$

$$I = \{\langle t_f \mid r \mid t_E\rangle + \langle t_f \mid r \mid w_E\rangle \,\text{Re} \tan(\delta_{\text{opt}} - \delta_n)\}\{1 - i \,\text{Re} \tan(\delta_{\text{opt}} - \delta_n)\}^{-1}. \tag{4.12}$$

We mentioned under Eq. (3.40) that

$$\text{Re}(\tilde{\omega}_{\lambda f}^{1/2}/\tilde{\omega}_{\lambda n}^{1/2}) = \tilde{\Gamma}_{\lambda f}^{1/2}/\tilde{\Gamma}_{\lambda n}^{1/2}, \tag{4.13}$$

$$\text{Im}\, \Gamma_{\lambda f}^{1/2}/\Gamma_{\lambda n}^{1/2} \propto -\langle t_f \mid r \mid t_E\rangle. \tag{4.14}$$

4.2. *Single-Particle Potential*

In all previous calculations based on the shell-model approach, the single-particle potential v_0 was taken equal to, or at least very close to, the real part of some phenomenological optical-model potential [5]. In particular, and in the present context, this was the case in [10–12]. This choice is related to the fact that this v_0 is close to the Hartree–Fock potential, which makes the matrix elements $V_m{}^n$ and V_{EE}^{nn} (see below Eq. (3.10)) vanish. However, the choice $v_0 = \text{Re (OMP)}$ may lead to misleading or erroneous results [10, 11] in the case of radiative capture at low energy, as we now discuss. In connection with Eqs. (3.34) and (3.35), we noted that the channel–channel coupling V_{EE}^{nn} plays no essential role in the valence capture model. Hence, it is not essential to choose v_0 in such a way that V_{EE}^{nn} vanishes. In fact, this choice may not be convenient in some cases: It yields $\tilde{K}_{nn}^{(0)} = 0$ (see Eq. (3.10)) but also gives, in general, $\tilde{K}_{nn}^{(\infty)} \neq 0$ (see Section 2.5). This is because (see Eqs. (2.7) and (2.28)) $\tilde{K}_{nn}^{(\infty)}$ contains, besides $\tilde{K}_{nn}^{(0)}$ the contribution of the tails of the "far-away" levels (i.e., of those other than λ). In other words, the background potential scattering phase shift in general differs from the model scattering phase shift δ_n if v_0 is chosen in such a way that $\tilde{K}_{nn}^{(0)} = 0$. This was emphasized by Lane and Mughabghab [12].

In the present context, there exist two main reasons to prefer a single-particle potential v_0 such that $\tilde{K}_{nn}^{(\infty)} = 0$ or, equivalently, that $\delta_n = \text{Re}\, \delta_{\text{opt}}$. The first one is that, according to Eq. (3.36) (or, equivalently, Eq. (4.12)), the background cross section is then equal to the direct capture cross section. The second, more important, reason is that (see Section 2.6) it is only for this choice that the partial width $\tilde{\Gamma}_{\lambda n}$ can be identified with the phenomenological neutron width. We return to these points in Sections 4.7, 5, and 6. However, we will see in Sections 4.3–4.5 that accurate results can also be obtained from the choice $v_0 = \text{Re OMP}$. This is related to the importance of external capture (see Sections 3.5 and 5.2).

At low energy, i.e., approximately below 100 keV, the condition $\delta_n = \text{Re}\ \delta_{opt}$ essentially amounts to the requirement that the single-particle potential v_0 reproduces the experimental scattering length a_{sc}. In Fig. 1, we show the dependence

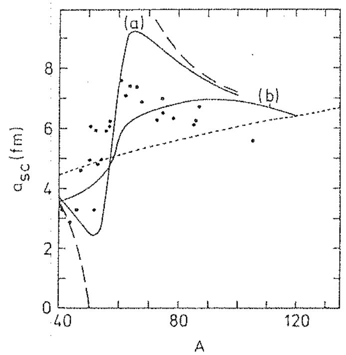

Fig. 1. Dependence of the scattering length on mass number. The short dashes represent the hard sphere value 1.3 $A^{1/3}$. The curves labeled (a) and (b) are computed from the OMP of [31] and [33], respectively. The long dashes are obtained from the real part of the OMP of [31]. The full dots show the experimental values, taken from [33].

upon A of the scattering length a_{sc}, defined as the limit for $k \to 0$ of the quantity $-k^{-1}\,\text{Re}(\delta_{opt})$, calculated from several optical-model potentials. In the case of [31], we used for the real part of the OMP that given by Ross *et al.*, and add a volume absorption part with strength 3.36 MeV, as in [3]. For simplicity, we refer below to this complex OMP as to that of [31]. We also used the OMP of [32], but do not show the results in order not to complicate Fig. 1 too much. Note that a_{sc} becomes infinite (and changes sign) for a real Woods–Saxon potential with constant depth (see long dashes) and standard radius. This is incompatible with the experimental data (dots), which lie close to Curve (b) (with, however, rather large error bars). Hence, a real potential well with radius $r_0 A^{1/3}$ and constant diffuseness can reproduce the experimental a_{sc} only if its depth varies with A. We have taken the typical values [31] $r_0 = 1.3$ fm, $a = 0.69$ fm and have calculated numerically the depth V_0 of a real Woods–Saxon potential, which yields the same scattering length as the phenomenological OMP. The dashes in Fig. 2 give the values of V_0 that reproduce the values a_{sc} of the OMP of [33] (i.e., Curve (b) in Fig. 1); the full curve in Fig. 2 corresponds to Curve (a) of Fig. 1, i.e., to the OMP of [31]. We mainly use the latter since it was adopted in [11, 12] and since it gives reasonable values of E_γ. Below, we call $P1$ and $P2$ the real potentials, which correspond in Fig. 2 to the full and dashed curves, respectively. Note that the depth V_0 first decreases when A grows. This cannot be extrapolated for all A

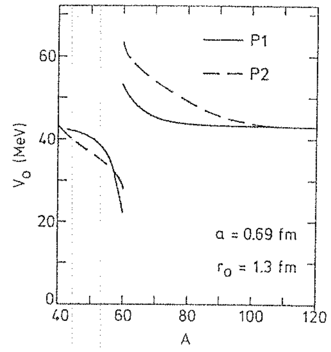

Fig. 2. Dependence on mass number of the depth of a real Woods–Saxon potential (radius 1.3 $A^{1/3}$, diffuseness 0.69 fm) which yields the same scattering as the OMP of [33] (long dashes) and of [31] (full curve), respectively.

without loss of meaning, since for $A \simeq 60$ a new 3s-bound state should be pulled inside the single-particle potential v_0, if it has to make any physical sense. Hence, we need to admit a discontinuity in the dependence of V_0 on A; however, despite this discontinuity, the scattering length remains continuous. Note that the discontinuity is quite large (20–30 MeV). We will see that it does not affect the calculated values. The exact value of A where the discontinuity occurs is somewhat arbitrary. We recall that the dependence of V_0 on A shown in Fig. 2 corresponds to the contribution to the scattering length of the tails of the distant levels.

In summary, it appears of interest to compare values calculated from three different single-particle potentials: (a) a complex OMP [1–4, 12]; (b) the real part of a standard complex OMP [10, 11, 22]; and (c) a real potential the depth of which depends discontinuously on A, as shown in Fig. 2. In the following sections, we mainly use as potential of Type (a) the OMP of [31], its real part as potential of Type (b), and the well $P1$ corresponding to the full curve in Fig. 2 as potential of Type (c).

4.3. *Dependence of Partial Widths on Mass Number*

4.3.a. *Thermal energy.* In Fig. 3, we plot the quantities $\Gamma_{\lambda f}/\Gamma_{\lambda n}$ and $\pi\Gamma_{\lambda f}/D$ at thermal energy. They are calculated from Eqs. (4.5) and (4.2). The curves labeled (a) correspond to the OMP of [31]; the OMP of [32] yields the curves labeled (b). In each case, the bound $2p\frac{3}{2}$ single-particle state t_f and the photon energy E_γ are calculated from the real part of the corresponding OMP. We see that the results are rather sensitive to the choice of the OMP, although the overall behavior of Curves (a) and (b) is the same. A closer look at the details of the numerical results shows that the main origin of the difference between Curves (a) and (b) is fairly

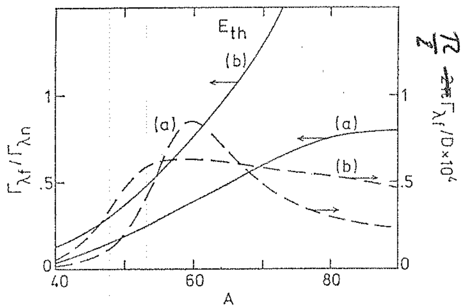

See note added in proof!

FIG. 3. Dependence on A of the quantities $\Gamma_{\lambda f}/\Gamma_{\lambda n}$ (left-hand scale) and $\pi\Gamma_{\lambda f}/D$ (right-hand scale) at thermal energy, as computed from Eqs. (4.5) and (4.2), respectively. The curves labeled (a) are calculated from the OMP of [31] and those called (b) are from the OMP of [32]. See note added in proof.

trivial: It lies in the factor E_γ^3 appearing in Eq. (4.3). In other words, the quantities J (Eq. (4.5)) are about the same for the OMP of [31] and [32]. In particular, the numerator of expression (4.5), and therefore, the reduced photon strength function $E_\gamma^{-3}\langle\Gamma_{\lambda f}\rangle/D$ (see Eq. (4.2)) is fairly insensitive to the OMP. Note that the values of E_γ calculated from the OMP of [31] are more realistic. In practice, E_γ is taken from experiment, rather than from the calculated energy of the bound $2p$-orbital (as we did in Fig. 3). Hence, the comparison of the experimental and theoretical values of $\Gamma_{\lambda f}/\Gamma_{\lambda n}$ does not crucially depend on the choice of the OMP. We return to this point in Section 4.3b.

At thermal energy, the background scattering phase shift vanishes. Hence, there exists no difference between the tilded and untilded reactance matrices (Section 2) when $\delta_n = \text{Re}\,\delta_{\text{opt}} = 0$ (see Eqs. (4.5)–(4.8)); moreover, then one has $\text{Im}\,\tilde{\omega}_{\lambda f}^{1/2}/\tilde{\omega}_{\lambda n}^{1/2} = 0$. However, if one takes $v_0 = \text{Re}\,(\text{OMP})$, then $\delta_n \neq \text{Re}\,\delta_{\text{opt}}$ and expression (4.6) can be very different from (4.5) (see Section 2.7). We illustrate this difference in Section 4.3.b. Finally, note that the neglect of the damping due to the photon channels is not justified above $A = 60$, at thermal energy.

4.3.b. *Partial widths at 100 keV.*

In Fig. 4, we plot the quantities $\Gamma_{\lambda f}/\Gamma_{\lambda n}$ and $\pi\Gamma_{\lambda f}/D$ versus A, at 100 keV. The conventions are the same as in Fig. 3: We use Eqs. (4.2) and (4.5), with the OMP of [31] (Curves (a)) and [32] (Curves (b)), respectively. By comparing Figs. 3 and 4, we see that the ratio $\Gamma_{\lambda f}/\Gamma_{\lambda n}$ is about 10^4 times smaller at 100 keV than at thermal energy. This is mainly due to the increase of $\Gamma_{\lambda n}/D$ with energy (see Fig. 14 below); indeed, we see that the quantity $\pi\Gamma_{\lambda f}/D$ has the same magnitude at thermal energy as at 100 keV. We return to this point in Sections 4.5 and 5 (see Figs. 16 and 20). Note that $\pi\Gamma_{\lambda f}/D$ shows a bump at about $A = 60$, followed by a plateau or a

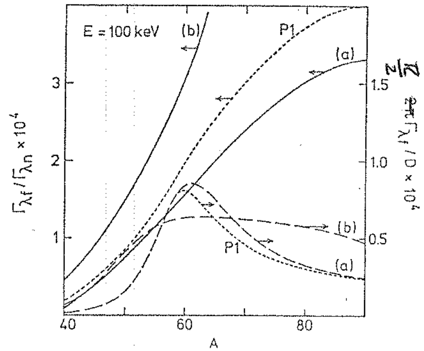

See note added in proof

FIG. 4. Dependence on A of the quantities $\Gamma_{\lambda f}/\Gamma_{\lambda n}$ and $\pi\Gamma_{\lambda f}/D$ at $E = 100$ keV. Same conventions as in Fig. 3 for the curves labeled (a) and (b). The short dashes are calculated from Eq. (4.6), with δ_n computed from the potential $P1$ of Fig. 2. See note added in proof.

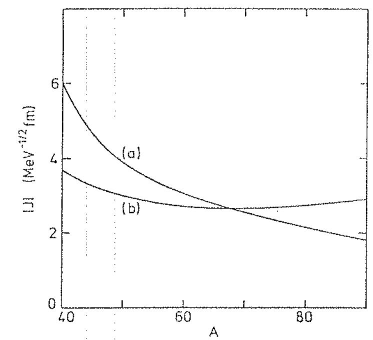

FIG. 5. Dependence on A of the quantity $|J|$ (Eq. (4.5)), for the OMP of [31] (Curve (a)) and of [32] (Curve (b)), respectively.

small decrease. Since the level distance is a rapidly decreasing function of A, this implies that $\Gamma_{\lambda f}$, i.e., the photon width in the valence capture model, first increases, reaches a maximum for A somewhat smaller than 60, and then decreases.

As we mentioned in Section 4.3.a, the main origin of the difference between Curves (a) and (b) in Fig. 4 lies in the binding energy of the $2p\frac{3}{2}$-level, which is larger in the case of Moldauer's OMP [32]; this difference between the E_γ values increases with A. In Fig. 5, we show the values of $|J|$ (Eq. (4.5)) for the OMP of [31] (curve (a)) and [32] (Curve (b)), respectively. We see that, as stated previously, these two curves are rather similar for the two OMP, particularly in the domain of interest ($45 < A < 65$). We now turn to the tilded partial widths (Eq. (4.6)). In the

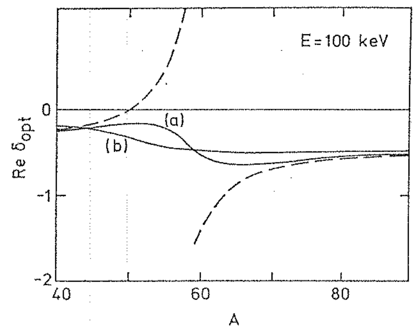

FIG. 6. Real part of δ_{opt} for the OMP of [31] (Curve (a)) and of [32] (Curve (b)) at 100 keV, versus A. The long dashes show the values of δ_n calculated from the real part of the OMP of [31].

present case, Re δ_{opt} takes small values as shown in Fig. 6. Hence, the values of δ_n at 100 keV, calculated from the real potential $P1$ shown in Fig. 2, barely differs from Curve (a). The short dashes in Fig. 4 represent the values of $\tilde{\Gamma}_{\lambda f}/\tilde{\Gamma}_{\lambda n}$ and of $\pi\tilde{\Gamma}_{\lambda f}/D$ as computed from Eq. (4.6), when δ_n is calculated from potential $P1$ of Fig. 2, while the optical-model quantities and E_γ are obtained from the OMP of [31]. We see that the dotted curves in Fig. 4 differ only little from the full Curves (a), i.e., that the tilded and untilded partial widths are about the same for this choice of δ_n.

The shell-model expressions for $\Gamma_{\lambda f}/\Gamma_{\lambda n}$ and $\tilde{\Gamma}_{\lambda f}/\tilde{\Gamma}_{\lambda n}$ are given by Eqs. (4.7) and (4.8), respectively. The function w_E (Eq. (3.31)) involves the quantity F (Eq. (3.30)) which has been calculated [11] only for $A = 56$ and $A = 60$ and for the special choice $v_0 = \text{Re(OMP)}$. However, we will see in Section 5.2 that the external capture dominates in the valence capture model, for the mass numbers of interest, Hence, we set here $F = 0$ in Eq. (3.31). We first discuss the values obtained when v_0 is identified with the real part of the OMP of [31], as was assumed in [11, 22]. The full curve labeled (a) in Fig. 7 shows the values of $\Gamma_{\lambda f}/\Gamma_{\lambda n}$ as computed from Eq. (4.7). Note that they are quite similar to those shown in Fig. 4, despite the wild variations of δ_n with A (see dashes in Fig. 6). We recall that the IR is defined by the cut-off radius a; here, we have set $a = 1.3A^{1/3}$. To gain an idea on the importance of internal capture and of the dependence of our results on a, we have also set a to zero, i.e., considered the whole space as the external region. Then, we obtain the values represented by Curve (b) in Fig. 7. We see that it is only for $A > 70$ that they differ appreciably from those represented by Curve (a). This implies that expression (4.7) is not sensitive to the choice of the cut-off radius a. The ratio $\tilde{\Gamma}_{\lambda f}/\tilde{\Gamma}_{\lambda n}$ calculated from Eq. (4.8), with $a = 1.3A^{1/3}$, is represented by the dash-and-dots in Fig. 7. We see that it differs very much from $\Gamma_{\lambda f}/\Gamma_{\lambda n}$ in the vicinity of $A = 60$, i.e., when $|\delta_n| \approx \pi/2$. Note here that the values calculated in

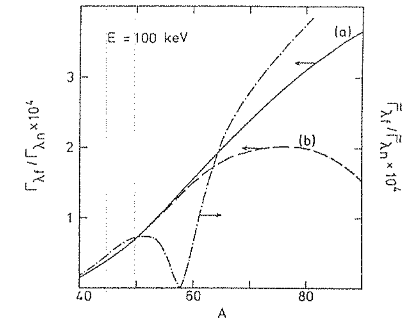

FIG. 7. Dependence on mass number of the quantities $\Gamma_{\lambda f}/\Gamma_{\lambda n}$ and $\tilde{\Gamma}_{\lambda f}/\tilde{\Gamma}_{\lambda n}$. All curves are computed from the real part v_0 of the OMP of [31]. Curve (a) corresponds to $\Gamma_{\lambda f}/\Gamma_{\lambda n}$ as calculated from Eq. (4.7) ($F = 0$), with the radius a of the IR taken equal to the potential radius (1.3 $A^{1/3}$); Curve (b) is also calculated from Eq. (4.7), but with $a = 0$. The dash-and-dots show the values of $\tilde{\Gamma}_{\lambda f}/\tilde{\Gamma}_{\lambda n}$, as obtained from Eq. (4.8) with $a = 1.3\ A^{1/3}$.

[11] correspond to $J = \langle t_f \mid r \mid t_E \rangle$ and are meaningless since the factorization assumption (see Eq. (3.27)) is incorrect in the (important) external region. Also recall that $\tilde{\Gamma}_{\lambda n}$ does not correspond to the phenomenological neutron width when δ_n differs from Re δ_{opt}, as is the case here for A close to 60 (see Fig. 6). Hence, no physical meaning can be directly attached to the dash-and-dots in Fig. 7.

In Fig. 8, we turn to the case when v_0 is identified with the real potential well $P1$ (see Fig. 2). The full curve labeled (a) in Fig. 8 shows the values of $\Gamma_{\lambda f}/\Gamma_{\lambda n}$ obtained from Eq. (4.7), with this choice of v_0 and with $F = 0$; the dashes labeled (a) cor-

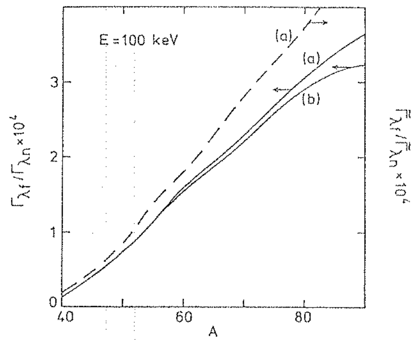

FIG. 8. Dependence on A of $\Gamma_{\lambda f}/\Gamma_{\lambda n}$ and of $\tilde{\Gamma}_{\lambda f}/\tilde{\Gamma}_{\lambda n}$ in the shell-model approach, when v_0 corresponds to the potential $P1$ in Fig. 2 and $a = 1.3\ A^{1/3}$. The full curve labeled (a) represents Eq. (4.7) and the dashes labeled (a) represent Eq. (4.8) ($F = 0$). The full curve (b) is obtained by dropping the contribution of the IR in Eq. (4.7).

respond to Eq. (4.8) ($F = 0$). In both cases, we took $a = 1.3A^{1/3}$. The curve labeled (b) is also obtained from Eq. (4.7) ($F = 0$) but now taking only the ER, i.e., limiting the integration over r to $r > 1.3A^{1/3}$. Note that the ER dominates and that the values of $\Gamma_{\lambda f}/\Gamma_{\lambda n}$ calculated from the OMP and from the shell-model approach are in fair agreement (compare Figs. 4 and 8).

Finally, we show in Fig. 9 some results concerning the ratio $\tilde{\omega}_{\lambda f}^{1/2}/\tilde{\omega}_{\lambda n}^{1/2}$. Its real part is equal to $\tilde{\Gamma}_{\lambda f}^{1/2}/\tilde{\Gamma}_{\lambda n}^{1/2}$. The full curves in Fig. 9 represent the values of $-\tilde{J}$ as calculated from Eq. (4.6); the OMP quantities are obtained from [31]. The full curve labeled (a) has been calculated with the phase shift δ_n corresponding to the real potential well $P1$ of Fig. 2; full Curve (b) corresponds to $v_0 = \text{Re OMP}$ [31]. The dashed curves labeled (a) and (b) represent the right-hand side of (4.14), for these two choices of v_0. Note that in the more meaningful case (a), the imaginary part of $\tilde{\omega}_{\lambda f}^{1/2}/\tilde{\omega}_{\lambda n}^{1/2}$ is much smaller than its real part. This implies that $\tilde{\Gamma}_{\lambda f}^{1/2}$ can be identified with the phenomenological photon width (see Section 2.7).

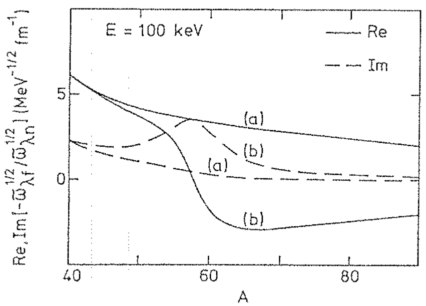

FIG. 9. Real (full curves) and imaginary (dashed curves) parts of $\tilde{\omega}_{\lambda f}^{1/2}/\tilde{\omega}_{\lambda n}^{1/2}$, after dividing by the kinematical factor contained in the braces in Eq. (4.3). Curves (a) correspond to the single-particle potential $P1$ of Fig. 2, while Curves (b) are obtained by taking v_0 equal to the real part of the OMP of [31].

4.4. *Background Cross Section*

The background cross section is given by Eq. (4.4), where the quantity I can be expressed in four different ways (Eqs. (4.9)–(4.12)). In the present section, we compare these various approximations with one another and also use several (real or complex) single-particle potentials. As in Section 4.3, we give results at thermal energy and, mainly, at 100 keV.

4.4.a. *Thermal energy.* At thermal energy, $\text{Re}\,\delta_{\text{opt}} = 0$ and expressions (4.9) and (4.10) are identical if $\delta_n = \text{Re}\,\delta_{\text{opt}}$. If, however, δ_n is calculated from the real part of some standard OMP, it can reach large values (see Fig. 6) and expressions (4.9) and (4.10) then become quite different (see Sections 2.7 and 3.6). This is

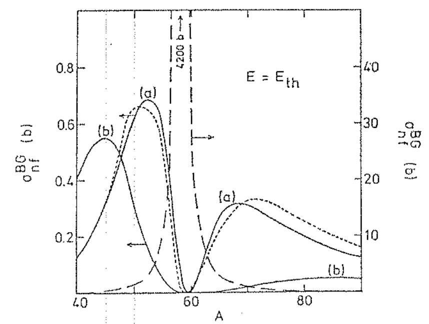

FIG. 10. Dependence on A of the background cross section, from several theoretical expressions. The full curves labeled (a) and (b) represent expression (4.9), with the OMP of [31] and [32], respectively. The two dashed curves correspond to $I = \langle t_f \mid r \mid t_E \rangle$: The long dashes are obtained by identifying v_0 with the real part of the OMP of [31]; the short dashes are obtained by taking for v_0 the potential $P1$ of Fig. 2.

illustrated in Fig. 10. Here, Curves (a) and (b) refer to Eq. (4.9), with the OMP of [31] and [32], respectively. Note that in the latter case the background cross section is negligible above $A = 55$. The large difference between Curves (a) and (b) beyond this value is related to the quantity I (Eq. (4.9)) and not to a trivial kinematical factor as in Fig. 3. The long dashes are obtained if one takes $I = \langle t_f \mid r \mid t_E \rangle$, with v_0 identified with the real part of the OMP of [31]. This dashed curve is proportional to the quantity called $\mid S^{\text{BG}} \mid^2$ in [16]; it cannot be identified with the background cross section σ^{BG} since $\tilde{K}_{nn}^{(\infty)} \neq 0$ [12]. The short dashes correspond to Eq. (4.12) where one takes for v_0 the potential $P1$ of Fig. 2. Note that the latter curve is in fair agreement with Curve (a) (see also Section 4.5.c).

4.4.b. *Background cross section at* 100 *keV*. The full curve labeled (a) in Fig. 11 represents σ^{BG} at 100 keV, as calculated from Eq. (4.9), with the OMP of [31]. The full curve (b) corresponds to Eq. (4.10), with $\delta_n = \text{Re}\,\delta_{\text{opt}}$ and the OMP of [31]. The long dashes give the direct capture value (3.36), for the cases when v_0 is the real part of the OMP of [31]. The short dashes represent Eq. (3.36), for the potential $P1$ of Fig. 2. In other words, the short dashes correspond to the shell-model expression (4.12) in which one makes $\tilde{K}_{nn}^{(\infty)} = \text{Re}\tan(\delta_{\text{opt}} - \delta_n) \simeq 0$. We recall that for the choice $v_0 = \text{Re OMP}$ made in [11, 16, 22], one has $\delta_n \neq \text{Re}\,\delta_{\text{opt}}$ (see Fig. 6) and Eq. (4.11) (or Eq. (4.12)) has to be used. The full curve in Fig. 12 shows the expression (4.11) in this case $v_0 = \text{Re OMP}$, for the OMP of [31]. We see that the overall agreement with the curves of Fig. 11 is good. This reflects the fact that the ER dominates (see Section 5.2), combined with the remark made under Eq. (3.61) that the ER contribution does not involve v_0 if the asymptotic form of the scattering states can be used. This does not hold true for Eq. (4.12) (see Eq.

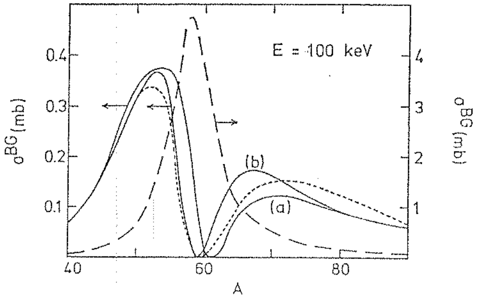

FIG. 11. Dependence of the background cross section on mass number. The full curves labeled (a) and (b) are obtained from Eqs. (4.9) and (4.10), respectively, with $\delta_n = \text{Re}\,\delta_{opt}$ and the OMP of [31]. Eq. (3.36) is represented by the long dashes in the case $v_0 = \text{Re OMP}$ and by the short dashes when v_0 is equal to the real potential $P1$ of Fig. 2.

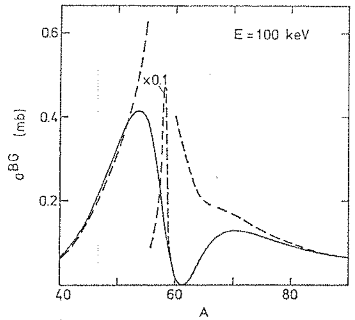

FIG. 12. Dependence of the background cross section on mass number. The full and the dashed curves are obtained from Eqs. (4.11) and (4.12), respectively, for a single-particle potential v_0 equal to the real part of the OMP of [31].

(3.61)), which is represented by the dashes in Fig. 12, for v_0 taken equal to the real part of the OMP of [31]. Clearly, Eq. (4.12), or equivalently Eq. (3.58), leads to meaningless results in this case. This can be interpreted in terms of the difference between assumptions (2.37a) and (2.37b) (see Sections 2.7 and 3.6). Assumption (2.37b) is not satisfactory for δ_n calculated from $v_0 = \text{Re OMP}$ since Re tan $(\delta_{opt} - \delta_n)$ is then a wild function of A (see Fig. 6), in contrast with the experimental data on the scattering length (see Fig. 1).

4.5. *Energy Dependence for $A = 60$*

In the present section, we study in some detail the energy dependence of the photon width and of the background cross section for $A = 60$. The comparison with experiment is postponed until Section 4.6.

4.5.a. *Phase shifts.* We mentioned in Section 4.2 that three single-particle potentials are of interest, namely the OMP, its real part, and a real potential such that its phase shift $\delta_n \approx \text{Re}\,\delta_{opt}$ (see Fig. 2). In the present section, we take the OMP of [31]. In Figs. 13 and 14, respectively, we plot the real and imaginary parts of the quantity $\tan(\delta_{opt} - \delta_n)$. The full curves correspond to $\delta_n = 0$; the long dashes correspond to δ_n equal to the phase shift δ_0 computed from $v_0 = \text{Re OMP}$; the dots are obtained when calculating δ_n from the real potential $P1$ of Fig. 2. Fig. 14 shows that for $E < 200$ keV the quantity $\text{Im}\tan(\delta_{opt} - \delta_n)$ does not crucially depend on the (real) value of δ_n. We recall that this imaginary part appears in the ratio $\tilde{\Gamma}_{\lambda f}/\tilde{\Gamma}_{\lambda n}$ (Eq. (4.6)). Therefore, we expect that the latter ratio is rather independent of δ_n, for $A = 60$ and in the energy range $E < 200$ keV. This is in agreement with the results shown in Fig. 4. We note that $\text{Re}\tan(\delta_{opt} - \delta_n)$ is quite different from $\text{Re}\tan(\delta_{opt})$ if $\delta_n = \delta_0$ (compare long dashes with full curve in Fig. 13). Hence, the background cross sections computed from Eqs. (4.9) and (4.10),

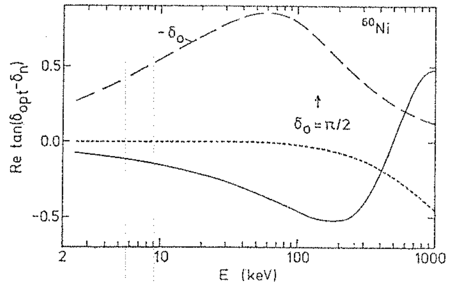

FIG. 13. Energy dependence of the real part of $\tan(\delta_{opt} - \delta_n)$, for the OMP of [31]. The full curve corresponds to $\delta_n = 0$, the long dashes represent δ_n $(=\delta_0)$ computed from $v_0 = \text{Re OMP}$ and the short dashes correspond to δ_n calculated from the real potential $P1$ of Fig. 2.

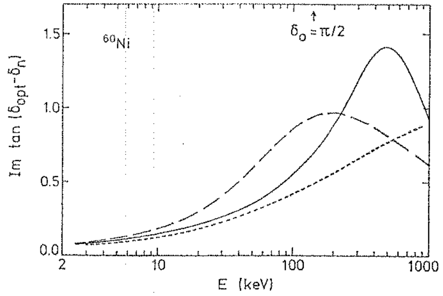

FIG. 14. Energy dependence of the imaginary part of $\tan(\delta_{opt} - \delta_n)$, with the same conventions as in Fig. 13.

respectively, are quite different for $v_0 =$ Re OMP; this was already apparent in Figs. 11 and 12. However, recall (see [12] and Section 4.4) that this choice $v_0 =$ Re OMP is unwise. In contrast, the potential shown in Fig. 2 yields a fair agreement between the shell-model and the optical-model approaches (see Sections 4.3, 4.4, 4.5.b, and 4.5.c).

4.5.b. *Photon width.* In the present section and in Section 4.6 below, the bound state t_f is calculated from the real part of the OMP of [31] and we take the experimental value of E_γ, namely $E_\gamma = E + 7.60$ MeV.

In Fig. 15, we show the energy dependence of the ratio $\Gamma_{\lambda f}/\Gamma_{\lambda n}$. The values calculated from the Lane–Mughabghab formula (4.5) and from the shell-model expression (4.7) *coincide* and are *both* represented by the full curve. Here, we took (in Eq. (4.7)) $v_0 =$ Re OMP, with the values of F given in [11]. The values of $\tilde{\Gamma}_{\lambda f}/\tilde{\Gamma}_{\lambda n}$ calculated from Eq. (4.6) on the one hand or from Eq. (4.8) on the other hand (for $v_0 =$ Re OMP) also *coincide* and are represented by the long dashes.

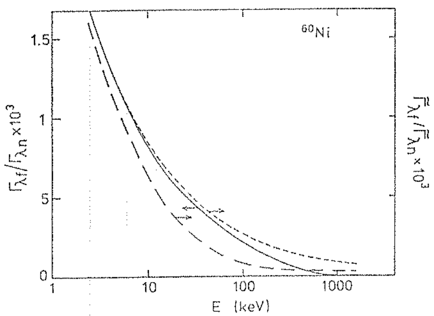

FIG. 15. The full curve represents the values of $\Gamma_{\lambda f}/\Gamma_{\lambda n}$ as calculated from Eq. (4.5) with the OMP of [31]; the difference between these values and the results obtained from Eq. (4.7) (with $v_0 =$ Re OMP) is so small that it cannot be shown on the drawing. The short dashes represent $\tilde{\Gamma}_{\lambda f}/\tilde{\Gamma}_{\lambda n}$ as obtained from Eq. (4.6), with δ_n ($\simeq$ Re δ_{opt}) calculated from the real potential $P1$ of Fig. 2. The long dashes show $\tilde{\Gamma}_{\lambda f}/\tilde{\Gamma}_{\lambda n}$ as obtained from Eq. (4.8) with $v_0 =$ Re OMP; these values cannot be distinguished graphically from those obtained from Eq. (4.6), with δ_n calculated from Re OMP.

Finally. the short dashes show the ratio $\tilde{\Gamma}_{\lambda f}/\tilde{\Gamma}_{\lambda n}$ as obtained from Eq. (4.6), where δ_n is calculated from the real potential $P1$ of Fig. 2, i.e., from a Woods–Saxon potential with depth 52.8 MeV. Note that all three curves take about the same values. Furthermore, the values calculated from the real potential $P2$ of Fig. 2, i.e., from a Woods–Saxon potential with depth 28.0 MeV, coincide with the short dashes in Fig. 15. These findings correspond to the remark made above in connection with Fig. 14 and to the fact that the ER dominates (see Section 5.2).

By multiplying $\Gamma_{\lambda f}/\Gamma_{\lambda n}$ by Im tan δ_{opt} or $\tilde{\Gamma}_{\lambda f}/\tilde{\Gamma}_{\lambda n}$ by Im tan$(\delta_{\text{opt}} - \delta_n)$, we obtain the curves shown in Fig. 16. As discussed at the beginning of Section 4.3.b (in connection with Figs. 3 and 4), we see that $\Gamma_{\lambda f}/D$ is approximately constant below 200 keV. It then decreases fairly rapidly. However, the more meaningful quantity $\tilde{\Gamma}_{\lambda f}/D$, which is represented by the short dashes in Fig. 16, decreases less rapidly. We recall that the long dashes are not *directly* related to the usual empirical definition of the photon width. We return to these results in Section 5.7.

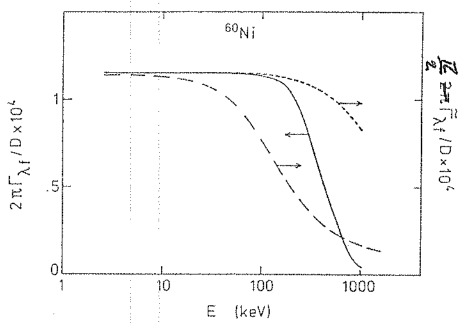

note added in proof

FIG. 16. Photon strength function $\pi\Gamma_{\lambda f}/D$ and $\pi\tilde{\Gamma}_{\lambda f}/D$, with the same conventions as in Fig. 15. See note added in proof.

4.5.c. *Background cross section.* The full curves and the short dashes in Figs. 10–12 show that the background cross section is very small for $A = 60$ below 100 keV. This makes one expect that σ^{BG} in this region can be very sensitive to the details of the potential or to the theoretical approximation which is used. In the present section, all optical-model quantities are computed from the OMP of [31]. The full curve in Fig. 17 shows the energy dependence of σ^{BG} calculated from the Lane-Mughabghab formula (4.9); the open squares are obtained from the corresponding shell-model expression (4.11), where δ_n is computed from the potential $v_0 =$ Re OMP. The dots are obtained from Eq. (4.11), with t_E, w_E, and δ_n calculated from the potential $P1$ of Fig. 2 ($F = 0$). Note the very good agreement; the deviation at low energy arises from the fact that the quantity I in Eq. (4.11) is then more sensitive to the value of the separation radius a (Eq. (3.31)). As expected from the dominance of the external region and from the discussion appearing below Eq. (3.61), these results are not sensitive to the choice of v_0 or of δ_n. This is not true for the value of σ^{BG} calculated from Eq. (4.10) or from the corresponding shell-model relation (4.12): When calculating δ_n from $v_0 =$ Re OMP, Eq. (4.10) yields the dashes and Eq. (4.12) yields the crosses in Fig. 17; the agreement between the two expressions is again very good, but the difference with expression (4.9) (or (4.11)) is large. As discussed in [12] and in Section 4.4.b, this choice of δ_n is not satisfactory, and it would be more realistic to calculate the value of (4.10) with

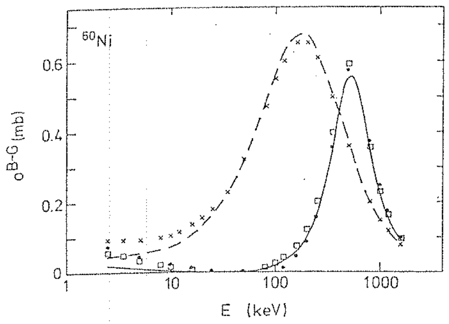

FIG. 17. Energy dependence of the background cross section for $A = 60$. In all cases, the OMP of [31] is used. The full curve represents the background cross section calculated from Eq. (4.9). The open squares are calculated from Eq. (4.11), where t_E, w_E, and δ_n are obtained from $v_0 = \text{Re OMP}$. The dashes and crosses represent Eqs. (4.10) (4.12), respectively. The full dots are obtained from Eq. (4.11), with t_E, w_E, and δ_n calculated from the potential $P1$ of Fig. 2 ($F = 0$).

$\delta_n = \text{Re}\ \delta_{\text{opt}}$ or the value of (4.12) with the real potential $P1$ of Fig. 2. The results obtained in this way are shown in Fig. 18 (note the enlarged scale with respect to Fig. 17). The full curve in Fig. 18 is obtained from Eq. (4.10), where δ_n is calculated from potential $P1$ of Fig. 2; the long dashes show the values of expression (4.12), with $F = 0$ and δ_n corresponding to $P1$; the short dashes represent the direct capture cross section (3.36), as calculated from $P1$. The difference between the long and short dashes above 10 keV is due to the fact that $\text{Re}\tan(\delta_{\text{opt}} - \delta_n)$ does not exactly vanish above a few keV, while the ratio $\rho = |\langle t_f \mid r \mid w_E \rangle| / |\langle t_f \mid r \mid t_E \rangle|$ is large: ρ is equal to about 100 at 10 keV and to about 20 at 200 keV. The difference between the short dashes in Fig. 18 and the full curve in Fig. 17 is due to the fact

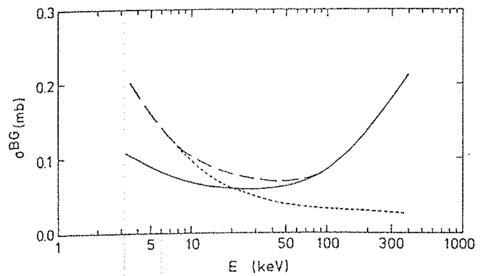

FIG. 18. Energy dependence of the background cross section for $A = 60$. The full curve is calculated from Eq. (4.10), and the long dashes are calculated from Eq. (4.12), with δ_n calculated from the potential $P1$ of Fig. 2; the OMP is that of [31]. The short dashes represent the direct capture cross section (3.36), calculated from $P1$.

that $\text{Re}\tan(\delta_{\text{opt}} - \delta_n)$ increases above 100 keV (see Fig. 13). The difference between the long dashes and the full curve in Fig. 18 below 100 keV has the same origin as the difference between the squares and the full curve in Fig. 17. Note that the cross section is very small in all cases and that the difference between the various theoretical expressions is of the same order as the differences that appear when using Eq. (4.9) (for instance) with different phenomenological OMP.

4.6. *Comparison with experiment*

In the previous sections, we compared with one another several expressions for the partial widths and for the background cross section. We showed that the shell-model and the optical-model approaches lead to practically equivalent results, provided that one makes a sensible choice for the model scattering phase shift. Once this is established and understood, one can rely on the most convenient approach for practical calculations. In Tables I and II, we compare the optical-model values (4.5) with experimental data in the cases ^{56}Fe(n, γ) and ^{60}Ni(n, γ), respectively. In the first column, we show the resonance energies, as quoted by Jackson and Strait [34]. The second column lists the experimental neutron [35] widths. In the third column, we quote the experimental photon widths given in (a) [34] and (b) [36], respectively. The fourth column gives the theoretical photon width $\Gamma_{\lambda f}$, as calculated from Eq. (4.5). The spectroscopic factors are obtained from [37]: $s_f^2 = 0.39$ for ^{60}Ni and $s_f^2 = 0.55$ for ^{56}Fe. The fifth column contains the values of $\tilde{\Gamma}_{\lambda f}$ as calculated from Eq. (4.6), where δ_n is obtained from the potential $P1$ of Fig. 2, i.e., with a potential of depth 52.8 MeV for ^{60}Ni and 37.5 MeV for ^{56}Fe. We took for E_γ the observed photon energy in both cases. Finally, the last column shows the values calculated in [38] from the R-matrix approach; their connection with the optical-model approach is discussed in [12], where it is mentioned that the values listed in the last column of Tables I and II should be corrected to take into account the finite diffuseness of the Woods–Saxon potential and the proper normalization of the scattering state ; these two corrections approximately cancel each other [12]. Note that the quantity $\gamma_{\lambda f}^2$ listed in [39] slightly differs from those given in Columns 4 and 5 of Table II because of their different definitions. Finally, we recall that the factor Z^2A^{-2} appearing in Eqs. (4.3) and (4.4) arises from the rather crude assumption that the effective charge of the valence neutron is $-eZ/A$. In view of this, we can conclude from Tables I and II that a fair agreement exists between the valence capture model and the experimental data, in both cases. More precisely, the significant fact is that the valence capture model of Lane and Lynn [1–4] yields the correct magnitude for the photon width. This indicates that the very small admixture of the valence configuration in the compound nuclear resonance dominates the dipole transition probability. We discuss this point in Section 5.

TABLE I

Resonance Parameters for ^{56}Fe(n, γ)

E_λ (keV)	$\Gamma_{\lambda n}$ (keV)	$\Gamma_{\lambda f}$ (eV) exp (a)	(b)	$\Gamma_{\lambda f}$ (eV) (Eq. (4.5))	$\tilde{\Gamma}_{\lambda f}$ (eV) (Eq. (4.6))	$\Gamma_{\lambda f}$ (eV) [38]
27.9	1.52	0.112	0.17	0.46	0.47	0.127
74.0	0.54	0.082	0.24	0.89	0.97	0.021
123.5	0.014	0.119		0.002	0.002	0.006
130.0	0.66	0.105	0.056	0.074	0.083	0.018
141.0	2.27	0.068	0.072	0.232	0.270	0.081
169.0	0.76	0.066	0.12	0.064	0.076	0.022
188.0	3.20	0.423	0.42	0.248	0.305	0.096

TABLE II

Resonance Parameters for ^{60}Ni(n, γ)

E_λ (keV)	$\Gamma_{\lambda n}$ (keV)	$\Gamma_{\lambda f}$ (eV) (exp)	$\Gamma_{\lambda f}$ (eV) (Eq. (4.5))	$\tilde{\Gamma}_{\lambda f}$ (eV) (Eq. (4.6))	$\Gamma_{\lambda f}$ (eV) [38]
12	1.91	0.367	0.570	0.590	0.390
43	0.14	0.018	0.021	0.023	0.006
98	1.07	0.102	0.095	0.115	0.045
108	1.75	0.209	0.140	0.175	0.030
162	5.30	0.166	0.296	0.450	0.051
186	5.70	0.062	0.274	0.455	0.227
190	3.50	0.557	0.168	0.280	0.114

4.7. *Discussion*

In Sections 4.3–4.6, we used three widely different average potential wells, namely a complex optical-model potential (OMP), the real part of this OMP, and finally a real potential well ($P1$) which reproduces the same scattering length as the complex OMP. Our numerical results lead to the following conclusions, which will be interpreted in Sections 5 and 6.

(a) The three potentials lead to practically the same values of the photon width $\Gamma_{\lambda f}$ (Eq. (2.8)). However, the relations derived in Section 2.5 must be used to derive $\Gamma_{\lambda f}$ from the "model" photon width $\tilde{\Gamma}_{\lambda f}$. We recall (Section 2.6) that $\tilde{\Gamma}_{\lambda f}$ (see Eq. (2.16)) is closest to the usual (empirical) photon width, provided that θ (which corresponds to δ_n in Eqs. (4.6)–(4.8)) is taken equal to the real part of $\tan \delta_{\text{opt}}$. Since $\text{Re} \tan \delta_{\text{opt}} \ll 1$ at low energy (see Figs. 6 and 13), the difference between this $\tilde{\Gamma}_{\lambda f}$ and $\Gamma_{\lambda f}$ is small in practice.

(b) All three potentials lead to practically the same value for the background cross section if one uses the same dynamical assumption (Eq. (2.37a) *or* Eq. (2.37b)). When the model background phase shift is large (which also implies that it varies rapidly with energy for fixed A and with mass number for fixed energy), assumption (2.37b) is not substantiated by the experimental data (see also Section 2.7). If one uses in the shell-model approach a real potential well that reproduces the observed scattering length (see Fig. 2) the background and the direct radiative capture cross sections coincide.

(c) The photon width calculated from the valence capture model shows a maximum somewhat below $A = 60$. It is approximately independent of energy below 100 keV, and then decreases.

(d) External capture appears to dominate in the valence capture model (see Fig. 8).

5. Validity of the Valence Capture Model

5.1. *Introduction*

In the present section, we discuss the conditions of validity of the valence capture model. This problem has been investigated recently by Lane and his collaborators [17, 41–43] in the frame of R-matrix theory. These authors studied two main questions [43]:

(a) Why is the whole dipole strength not contained in the giant dipole resonance (GDR) [42]?

(b) Why do the low-lying excited states of the target apparently play a negligible role in the capture process, at least for certain ranges of values for A [40, 41]?

We organize our discussion as follows. In the present section, we make a brief comment on the nature of Problems (a) and (b). In Section 5.2, we show quantitatively the extent to which external capture dominates in the valence capture model [2–4, 17, 30]. As before, we study the region $40 < A < 80$ as a specific example. We discuss Problem (a) in Section 5.3. In Sections 5.4–5.9, we turn to Problem (b). Besides discussing the latter problem quantitatively in the frame of the shell-model approach we endeavor to establish some contact with the R-matrix theory. Section 5.10 contains a brief discussion.

The nature of Problem (a) is the following. The schematic model [44] predicts that practically all the dipole strength at low energy is transferred to the GDR. This is confirmed by detailed shell-model calculations. How can this be reconciled with the success of the valence capture model that shows that part of the strength may remain located near neutron threshold (at least)? This is discussed in Sections 5.3 and 5.10.

Problem (b) can be phrased as follows. We decompose the final state Ψ_f reached after photon emission (see Eq. (2.6)) into configurations where the target appears in its ground state ψ_t (see Eqs. (3.1) and (3.31), spectroscopic factor s_f), in its first excited state ψ_1 (spectroscopic factor s_1), etc. As before, we ignore antisymmetrization [40]:

$$\Psi_f = s_f \psi_t t_f + s_1 \psi_1 t_f + \cdots \tag{5.1}$$

Only the configuration with "large" spectroscopic factors needs to be retained in this expansion. In the valence capture model, only the contribution of the first term on the right-hand side of Eq. (5.1) to the dipole transition probability is taken into account. At first sight, this appears unjustified in the cases [41, 43] where $s_1^2 > s_f^2$ (for instance).

5.2. *Dominance of External Region*

It has been emphasized repeatedly in the literature [2–4, 17, 30, 43] that external capture dominates in the valence capture model. In other words, the photon is most often emitted while the neutron is outside the nucleus, i.e., in the external region (ER). To obtain a quantitative evaluation of the importance of external capture, we have calculated the ratio of the contribution of the internal region to the full contribution, for the background cross section (dashes in Fig. 19) and for the photon width (full curve in Fig. 19), respectively. We used the Lane–Mughabghab expressions (4.5) and (4.9), and the OMP of [31] (with the imaginary part of [3]). The peak in the dashed curve near $A = 62$ simply reflects the fact that σ^{BG} vanishes there, and is of no interest in the present context. Note that more than 99% of the photon width arises from external capture. Below, we argue that this is sufficient to explain the success of the valence capture model (see discussion in Section 5.10). However, other factors may, play some role as well; a model embodying the possible coexistence of several effects is being investigated presently by Lane [43, 45].

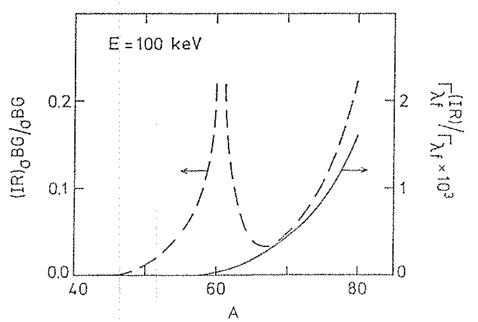

FIG. 19. Ratio of the contribution of the internal region to the full valence capture value. The long dashes (left-hand scale) correspond to the background cross section calculated from Eq. (4.9). The full curve (right-hand scale) corresponds to the photon width (Eq. (4.5)). The OMP is that of [31].

Note that the contribution of the ER to the photon width (Eq. (3.52)) can be obtained easily [2–4] without recurring to any particular formalism. From Eqs. (2.3) and (2.7), we have, assuming that the asymptotic form is valid in the whole ER,

$$u(r, E) = \left(\frac{2}{\pi \hbar v}\right)^{1/2} \left[\sin kr + K_{nn}^{(0)} \cos kr + \frac{1}{2} \sum_{\lambda} \frac{\Gamma_{\lambda n}}{E_\lambda - E} \cos kr\right]. \tag{5.2}$$

Eqs. (2.6) and (2.8) then yield

$$\Gamma_{\lambda f}^{(\mathrm{ER})} = -s_f \left(\frac{2}{\pi \hbar v}\right)^{1/2} \Gamma_{\lambda n}^{1/2} \langle t_f \mid d \mid \cos kr \rangle_{\mathrm{ER}}\,. \tag{5.3}$$

5.3. *Decoupling from the Giant Dipole Resonance*

The derivation of Eq. (5.3) shows that the valence model contribution $\Gamma_{\lambda f}^{(\mathrm{ER})}$ is unavoidably present, regardless of the existence of a GDR. In other words, the GDR can concentrate all the dipole strength available in the IR but can do nothing about the external region part, which is dominant in the valence capture model. Another way to state this is the following. In the schematic model the particle-hole nuclear interaction is replaced by a dipole–dipole force. In view of the short-range nature of the residual nuclear interaction this model is meaningful in the IR only. Hence, we believe that the dominance of the ER alone is sufficient to explain that the dipole strength corresponding to valence capture remains located at low energy. This does not exclude the possible existence of other effects [42, 43]. From Figs. 15 and 16, and also from Sections 5.4–5.8 below, we see that this "residual" dipole strength is restricted to the vicinity of the neutron threshold, and therefore only gives a very small contribution to the dipole sum rule. Finally, Figs. 4 and 5 show that the valence capture contribution reaches a maximum near the peak of the neutron strength function. We return to this point in Section 5.10.

Precisely because of this decoupling from the ER, the GDR plays an important role in the success of the valence capture model at low energy. Indeed, the GDR transfers most of the dipole strength contained in the IR to higher energy, so that the contribution to the photon width amplitude of the first term on the right-hand side of Eq. (3.13) can be small compared to the valence model value, i.e., to the entrance channel contribution to the second term on the right-hand side of Eq. (3.13).

5.4. *Contribution of the Low-Lying Excited States of the Target to the Photon Width*

The contribution of the excited state ψ_1 of the target (second term in Eq. (5.1)) appears in Eq. (3.13) and reads

$$\Gamma_{\lambda f}^{1/2}(1) = \pi^{-1} s_1 Y_1(E - \epsilon_1), \tag{5.4}$$

where ϵ_1 is the threshold energy (excitation energy of ψ_1), while

$$Y_1(E - \epsilon_1) = \int_{\epsilon_1}^{\infty} dE' \, (E - E')^{-1} F_1(E'), \tag{5.5}$$

$$F_1(E') = \langle \xi_\lambda \mid \bar{V} \mid \chi_{E'}^{\epsilon_1} \rangle \langle t_{E''}^{\epsilon_1} \mid d \mid t_f \rangle, \tag{5.6}$$

$$E'' = E' - \epsilon_1 . \tag{5.7}$$

Here, we assumed for simplicity that no bound state ϕ_m need be introduced (see Section 5.6 below).

The main properties of the functions $F_1(E')$ and $Y_1(E - \epsilon_1)$ are the following [46], in the one-particle case:

(i) The quantity $F(E')$ behaves like $(E' - \epsilon_1)^{l+1/2}$ for the lth partial wave in $t_{E''}^{\epsilon_1}$.

(ii) The function $Y_1(E - \epsilon_1) \to 0$ for $E \to -\infty$ if $F_1(E')$ is square integrable.

(iii) The function $Y_1(E - \epsilon_1)$ is continuous at $E = \epsilon_1$.

(iv) For $l = 0$, dY_1/dE is discontinuous at $E = \epsilon_1$. It is infinite for $E \to \epsilon_1 - 0$ and finite for $E \to \epsilon_1 + 0$; the derivative dY_1/dk_1, where

$$k_1 = \{(2M/\hbar^2) | E - \epsilon_1 | \}^{1/2}, \tag{5.8}$$

vanishes for $E \to \epsilon_1 + 0$ and differs from zero for $E \to \epsilon_1 - 0$.

These properties are interpreted and illustrated in Sections 5.5, 5.7, and 5.8 below. They are reminiscent of those of the shift function ($\mathscr{S}$) in R-matrix theory.

5.5. *Coordinate Space Representation*

The basic expression for the photon width amplitude in the shell-model approach is (3.13). In keeping with the findings of Sections 5.2 and 5.3, we restrict the discussion to the contribution of the external region (ER) to the matrix elements of the

dipole operator in Eq. (3.13). We assume that the compound state ξ_λ is entirely contained in the internal region. Then, the contribution of channel c to $\tilde{\Gamma}_{\lambda f}^{1/2}$ reads

$$\tilde{\Gamma}_{\lambda f, c}^{1/2(\text{ER})} = (2/\pi)^{1/2} \left\{ \int_{\epsilon_c}^{\infty} dE' \, \langle \Psi_f \mid d \mid \chi_{E'}^c \rangle_{\text{ER}} \langle \chi_{E'}^c \mid \bar{V} \mid \xi_\lambda \rangle_{\text{IR}} (E - E')^{-1} \right\}$$
$$+ (E - E_m)^{-1} \langle \Psi_f \mid d \mid \phi_m \rangle_{\text{ER}} \langle \phi_m \mid \bar{V} \mid \xi_\lambda \rangle_{\text{IR}} , \tag{5.9}$$

since in practice at most one bound state ϕ_m is associated with c (see, however, Section 5.6). The central quantity is thus the Green's function

$$G_E^{(c)}(r, r') = P \int_{\epsilon_c}^{\infty} dE' \, (E - E')^{-1} \chi_{E'}^c \rangle \langle \chi_{E'}^c + (E - E_m)^{-1} \phi_m \rangle \langle \phi_m . \tag{5.10}$$

Eq. (5.10) gives the bilinear expansion of the Green's function. Another representation of $G_E^{(c)}$ was used in Eq. (3.23), for an open channel ($E > \epsilon_1$). We first return to this case and then discuss the example of a closed channel.

(1) *In an open channel*, we write, with standard notation, in the one-particle case

$$G_E(r_<, r_>) = \frac{2M}{\hbar^2} \frac{u_E(r_<) \, C_E(r_>)}{W(u_E, C_E)}, \tag{5.11}$$

where we dropped the channel index and introduced the wronskian

$$W(f, g) = f(dg/dr) - g(df/dr), \tag{5.12}$$

which is independent of the value of r, where it is calculated since here both f and g are solutions of the radial single-particle wave equation with a local potential. In Eq. (5.11), $u_E(r)$ vanishes at $r = 0$, and C_E is proportional to $\cos(kr + \delta)$ at large r. Note the normalizations of u_E and of C_E are arbitrary. Two normalizations are of interest.

(i) We take, as in Eqs. (3.23), (3.24), and (3.31),

$$C_E(r) \sim \left(\frac{2}{\pi \hbar v}\right)^{1/2} \cos(kr + \delta) \qquad (r > a), \tag{5.13}$$

$$u_E(r) = t_E(r) \qquad (r < a). \tag{5.14}$$

Then we have (see Eqs. (2.1) and (5.13)):

$$W(u_E, C_E) = -2M/(\pi \hbar^2), \tag{5.15}$$

$$G_E(r, r') = -\pi C_E(r_>) \, t_E(r_<) \tag{5.16}$$

as stated in Eq. (3.23). This normalization corresponds to the shell-model expression for $\tilde{\Gamma}_{\lambda f}^{(\mathrm{ER})}$ and appears best suited for the treatment of the (dominant) ER in the elastic channel, provided that the potential v_0 is suitably chosen (see Sections 4.2 and 5.6).

(ii) We normalize $u_E(r)$ to unity in the internal region ($r < a$) and call this function $X_E(r)$, by analogy with R-matrix theory [15]. In the internal region, the quantities $X_E(r)$ and $X_E'(r)$ are approximately independent of energy in an energy interval small compared to the depth of v_0, i.e., over a few MeV (see Eq. (3.27) and Section 5.8). We take

$$C_E \sim \cos(kr + \delta) \qquad \text{for} \quad r \to \infty. \tag{5.17}$$

We assume that this asymptotic form can be used for $r > a$. This yields, for $r_< < a$ and $r_> > a$,

$$G_E(r, r') = -\frac{2M}{\hbar^2}\frac{\sin(ka + \delta)}{kX(a)} X(r_<) \cos(kr_> + \delta). \tag{5.18}$$

For $k \to 0$, we have

$$\delta \simeq -ka_0, \tag{5.19}$$

where a_0 is the potential scattering length corresponding to v_0. Eq. (5.18) confirms statements (iii) and (iv) of Section 5.4. It has the merit of displaying the threshold behavior more explicitly than Eq. (5.16) or, equivalently, than Eq. (3.23).

The difference between the two forms (5.16) and (5.18) of the single-particle Green's function is reminiscent of the difference between the treatment of continuum states in the R-matrix and shell-model approaches, respectively. In the former, one introduces a set of normalized states in the IR; one then diagonalizes H in that region and extrapolates toward the ER. In the shell-model approach, one normalizes the scattering states at large distance (see Eqs. (3.1) and (5.13)) and extrapolates towards the IR. We return to these similarities and differences in Section 5.9 below.

(2) *In a closed channel*, we call κ the quantity

$$\kappa = |k| = \{(2M/\hbar^2)(\epsilon - E)\}^{1/2}. \tag{5.20}$$

We use the functions

$$u_E(r_<) = X_E(r_<), \tag{5.21}$$

$$C_E(r_>) \sim e^{-\kappa r_>} \qquad (r_> \to \infty). \tag{5.22}$$

As before, X_E is normalized to unity in the IR. We assume that the asymptotic form (5.22) holds for $r_> > a$. By analogy with R-matrix theory [15], we introduce the notation

$$B = (aX_E'/X_E)_{r=a}, \qquad \mathcal{S} = -\kappa a. \tag{5.23}$$

We find, for $r_> > a$ and $r_< < a$,

$$G_E(r, r') = -(2Ma/\hbar^2)(B - \mathcal{S})^{-1}(X(r_<)/X(a))\, e^{-\kappa(r_> - a)}. \tag{5.24}$$

Before comparing the closed channel with the open channel contribution to the photon width, we devote a brief section to the choice of v_0 and the role of the bound states ϕ_m (see Eq. (5.10)).

5.6. *Bound States ϕ_m*

The Green's function (5.11) contains the influence of the bound single-particle states (see ϕ_m in Eq. (5.12)). That is the main reason why we treated ϕ_m on a separate footing from ϕ_j in Eq. (3.2). However, these states ϕ_m only have a small influence on $G_E(r, r')$ in an open channel, provided that $E - E_m >$ a few MeV. This is derived from the fact that the states ϕ_m are normalized to unity in all space. Thus, for $E - E_m >$ a few MeV, we can treat the bound states ϕ_m on the same footing as the ϕ_j while still using expression (3.23) (or (5.16)) in an open channel. Treating ϕ_m and ϕ_j on the same footing would also provide a better description of the compound states ξ_λ (see Eq. (3.7)), although this makes little difference in practice. In a closed channel, $G_E(r, r')$ has a pole at $E = E_m$; this is related to the factor $(B - \mathcal{S})^{-1}$ in Eq. (5.24). We encounter here a problem entirely analogous to the one associated with single-particle resonances in the shell-model approach [5.47]. This bound state pole is spurious, in the sense that it is cancelled by poles that appear elsewhere, for instance, in the quantities $\tilde{E}_\lambda$ and $\tilde{\Gamma}_{\lambda c}$ in Eq. (11). However, in the present context, it is not necessary to discuss this problem further for the following main reason. We saw in Section 4.2 that the most meaningful choice for v_0 for the description of radiative capture at low energy is such that $a_0 \simeq a_{\mathrm{sc}}$. Then, no weakly bound state ϕ_m occurs close to threshold (see Fig. 2 and also Section 5.8 below).

5.7. *Energy Dependence of the Photon Width*

Here we discuss the dependence on the distance of the resonance energy from threshold of the channel contributions to the photon width amplitude. We first discuss the open (elastic) channel contribution and then that of a closed channel.

(1) Let n denote the *open* (elastic neutron) channel. As in Sections 3 and 4, we usually drop this channel index, unless useful. Since $X(r_<)$ is independent of energy in the domain of interest (a few hundred keV above threshold), and since k is small, we can use Eq. (5.19). Fig. 13 shows that this is accurate up to about 200 keV. We find that the contribution to the ER of the elastic neutron channel n to the photon width amplitude has the form

$$\Gamma_{\lambda f,n}^{1/2} = K_\lambda^{(n)} s_f (a - a_0)\langle t_f \mid d \mid \cos k(r_> - a_0)\rangle_{\mathrm{ER}}. \tag{5.25}$$

Here, $K_\lambda^{(n)}$ is a quantity that depends on the structure of ξ_λ but not on resonance energy: It plays a role similar to that of the reduced neutron width amplitude in R-matrix theory [15]. The characteristic feature of the right-hand side of Eq. (5.25) is that it is independent of energy as long as

$$| k(a - a_0)| \ll 1. \tag{5.26}$$

The lowest order correction to (5.26) is proportional to k^2, and reads

$$[1 - \tfrac{1}{6}k^2(a - a_0)^2]\langle t_f \mid d \mid 1 - \tfrac{1}{2}k^2(\langle r\rangle - a_0)^2\rangle_{\mathrm{ER}}\,, \tag{5.27}$$

where $\langle r\rangle$ is the value of r where the integrand of $\langle t_f \mid d \mid 1\rangle$ is maximum. Eq. (5.27) shows that $| \Gamma^{1/2}_{\lambda f,n} |$ drops with increasing energy. Its derivative with respect to k vanishes as $k \to 0$, in keeping with Statement (iv) of Section 5.4 and with Fig. 16.

(2) The contribution of a *closed* channel 1 (with threshold energy ϵ_1) to the photon width amplitude can be written as follows (Eqs. (3.13), (5.5)–(5.7), and (5.24)):

$$\Gamma^{1/2}_{\lambda f,1} = \langle t_f \mid d \mid G_E^{(1)}(r, r')\, \psi_1 \bar{V} \mid \xi_\lambda\rangle$$
$$\Gamma^{1/2}_{\lambda f,1} = K_\lambda^{(1)} a^{-1} s_1 (B_1 - \mathscr{S}_1)^{-1} \langle t_f \mid d \mid \exp[-\kappa_1(r - a)]\rangle_{\mathrm{ER}}\,.$$

Since B_1 is nearly independent of energy, we can evaluate it at $\kappa_1 = 0$. This yields

$$B_1 = a/(a - a_0). \tag{5.28}$$

Thus, the quantity B_1 is independent of the channel index. Eq. (5.27) becomes

$$\Gamma^{1/2}_{\lambda f,1} = K_\lambda^{(1)} s_1(a - a_0)[1 + \kappa_1(a - a_0)]^{-1}\langle t_f \mid d \mid \exp - \kappa_1(r - a)\rangle_{\mathrm{ER}}\,.$$

Note that $K_\lambda^{(1)}$ contains a factor $[X(a)]^{-1}$ that has a pole for $a = a_0$, so that $\Gamma^{1/2}_{\lambda f,1}$ remains different from zero for $a \to a_0$. For $K_\lambda^{(1)} = K_\lambda^{(n)}$ and $s_1 = s_f$, we have $\Gamma^{1/2}_{\lambda f,c} = \Gamma^{1/2}_{\lambda f,n}$ at $k = \kappa_1 = 0$ (see Property (iii) of Section 5.4). We write

$$\Gamma^{1/2}_{\lambda f,1} = \alpha_\lambda^{(1)}\, [1 + \kappa_1(a - a_0)]^{-1}\, M_1 \tag{5.29}$$

where

$$M_1 = \langle t_f \mid d \mid \exp[-\kappa_1(r - a)]\rangle_{\mathrm{ER}}\,. \tag{5.30}$$

Expression (5.29) fulfills Statement (iv) of Section 5.4 since

$$\left[\frac{1}{\Gamma^{1/2}_{\lambda f,1}}\, d\Gamma^{1/2}_{\lambda f,1}/d\kappa_1\right]_{\kappa_1 = 0} = a_0 - a - \frac{\langle t_f \mid d \mid (r - a)\rangle_{\mathrm{ER}}}{\langle t_f \mid d \mid 1\rangle_{\mathrm{ER}}}\,. \tag{5.31}$$

Typically, the integrand in $\langle t_f \mid d \mid 1\rangle$ is maximum for $r - a \simeq 2.5$ fm. Eq. (5.31)

and Fig. 1 show that the decrease of $| \Gamma^{1/2}_{\lambda f,c} |$ with increasing distance from threshold is significant for $A < 60$ ($a_{sc} < a$), but becomes much slower for $A > 60$ ($a_{sc} > a$), when v_0 is chosen in such a way that $a_0 \simeq a_{sc}$ (see Section 4.2). This will be confirmed in Section 5.8 below by a few numerical examples. Hence, we expect that the role of the closed channels increases with increasing A. Above $A \simeq 60$, each of these closed channels may contribute as much as the elastic channel to $\Gamma^{1/2}_{\lambda f}$, for comparable spectroscopic factors and distance from threshold. For $A \simeq 50$ on the contrary, Eq. (5.30) shows that the damping (due to the distance from threshold) of the closed channel contribution to the photon width amplitude is, for

$$| \kappa_1(a - a_0)| \ll 1, \tag{5.32}$$

given by the quantity

$$H_1 = 1 - \kappa_1[(a - a_0) + (\langle r\rangle - a)] \simeq 1 - \kappa_1(\langle r\rangle - a_0), \tag{5.33}$$

with $\langle r\rangle \simeq a + 2.5$ fm.

Finally, note that our estimate of H_1 takes into account the dependence of M_1 (Eq. (5.30)) upon κ_1. When this (sizable) effect is neglected [41], we obtain

$$\left[\frac{1}{\Gamma^{1/2}_{\lambda f,c}}\, d\Gamma^{1/2}_{\lambda f,c}/d\kappa_1\right]_{\kappa_1 = 0} = a_0 - a \tag{5.34}$$

instead of Eq. (5.31).

5.8. *Numerical Results*

Here we illustrate the formulas derived in Section 5.7 and, by the same token, we check their accuracy. We drop the resonance and channel indices and use the following single-particle model for calculating the function Y in Eqs. (5.5) — (5.7):

$$Y(E - \epsilon) = \int_\epsilon^\infty dE'\, (E - E')^{-1} \langle f \mid t_{E''}\rangle_{\mathrm{IR}} \langle t_{E''} \mid d \mid t_f\rangle_{\mathrm{ER}}\,, \tag{5.35}$$

where the function $f(r)$ is taken equal to

$$f(r) = \exp[-(r - 0.8a)^2]. \tag{5.36}$$

As before, a denotes the potential radius ($1.3A^{1/3}$); it also defines the size of the IR. We checked that the shape of the calculated values of Y is fairly independent of the precise choice of $f(r)$.

The full curve in Fig. 20 shows the calculated value of $Y(E - \epsilon)$ for $A = 50$, when computing the scattering state t_E from the potential $P1$ of Fig. 2. The value of Y is normalized to unity at $E = \epsilon$. We also computed Y for $A = 45$ and $A = 55$

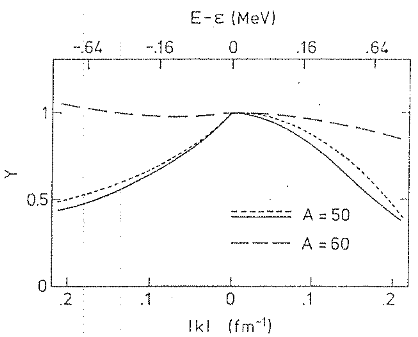

Fig. 20. Plot of the function $Y(E-\epsilon)$ (Eq. (5.35)) versus $|k|$ and $E-\epsilon$ for $A=50$ (full curve) and $A=60$ (long dashes). The function t_{E^*} in Eq. (5.35) is calculated from the real potential $P1$ of Fig. 2. The short dashes represent a two parameter fit to the full curve, with the expressions (5.37) and (5.38).

and found results close to those shown here for $A=50$. The short dashes in Fig. 20 represent a two-parameter fit to the full curve, using the following expressions, derived from Eqs. (5.26) and (5.29)

$$Y(E-\epsilon)=[1+\kappa(\langle r\rangle-a_0)]^{-1}, \qquad \text{for} \quad E<\epsilon, \tag{5.37}$$

$$Y(E-\epsilon)=1-\tfrac{1}{6}k^2[(a-a_0)^2+3(\langle r\rangle-a_0)^2], \qquad \text{for} \quad E>\epsilon. \tag{5.38}$$

The fit yields

$$a-a_0=2.4\text{fm}; \qquad \langle r\rangle-a=2.6\text{fm}. \tag{5.39}$$

These numbers are in good agreement with the value of $a-a_0$ appearing in Fig. 1 and with the expected value of $\langle r\rangle$ (see Section 5.7).

The long dashes in Fig. 20 represent the calculated value of Y for $A=60$. As expected from the facts that (Fig. 1) $a_0\simeq a+1$fm and that $\langle r\rangle$ decreases with increasing A (because of the larger binding energy of t_f), the value of Y is almost independent of energy for $A=60$. For $E>\epsilon$, this is in agreement with the result shown in Fig. 16 (short dashes). For $E<\epsilon$, this indicates that the contribution of a closed channel is for $A=60$ as important as that of the elastic channel, for equal spectroscopic factor and for equal distance from threshold.

This situation is expected to persist for $A>60$, since the experimental values of a_{sc} remain about 2 fm larger than a (see Fig. 1). The calculated values of Y for $A=70$ are shown in Fig. 21. The full curve is obtained from the potential $P1$ of Fig. 2, i.e., from the one that yields Curve (a) in Fig. 1. The rise of $Y(E-\epsilon)$ for $E<\epsilon$ reflects the existence in $P1$ of a bound state ϕ_m (see Section 5.6), with binding energy 1.45 MeV. Note that the scattering length corresponding to $P1$ is too large (see Curve (a) in Fig. 1) for $A=70$; the potential $P2$ (see Figs. 1 and 2)

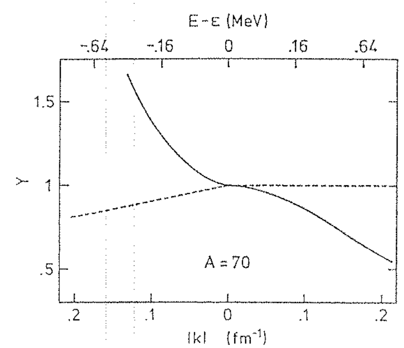

Fig. 21. Plot of the function $Y(E-\epsilon)$ (Eq. (5.35)) versus $|k|$ and $E-\epsilon$, for $A=70$. The full curve and the short dashes are calculated from the potentials $P1$ and $P2$ of Fig. 2, respectively,

gives more satisfactory values. This potential $P2$ is deeper than $P1$ for $A>60$. Hence, the single-particle bound state in $P2$ lies deeper (5.66 MeV) than in $P1$ and does not influence the calculated value of Y near threshold, as shown by the short dashes in Fig. 21. This supports the argument presented in Section 5.6.

In conclusion, the contribution of the low-lying excited states of the target can be as large as that of ground state for $A>60$, if these excited states have large spectroscopic factors. Since their contribution is not correlated with the neutron partial width, the occurrence of nonstatistical effects above $A=60$ is inhibited. However, note that the valence capture model can still give the right order of magnitude for the photon width in that region, even though the correlation between neutron and photon width is washed out.

5.9. *R-Matrix Formulation*

In Sections 5.5–5.8, we expressed the threshold effects in terms of the difference between the scattering length and the potential radius. Here, we relate these quantities to those appearing in R-matrix theory. This may for instance facilitate the comparison with the recent work by Lane [41].

In the usual R-matrix theory of optical-model potential, one introduces the one-level approximation [4],

$$R^{(\infty)}+i\pi\rho=\frac{\gamma_j^2}{\mathscr{E}_j-E+iW}, \tag{5.40}$$

which is assumed to hold in the vicinity of a single-particle state with energy $\mathscr{E}_j$ and with reduced width γ_j^2. The quantity ρ is the strength function; the quantity $R^{(\infty)}$ is related to the scattering length by [4],

$$a_{sc}\simeq a(1-R^{(\infty)}). \tag{5.41}$$

From Eqs. (5.40) and (5.41), we obtain

$$a - a_{sc} \simeq a \frac{(\mathscr{E}_j - E)\,\gamma_j^2}{(\mathscr{E}_j - E)^2 + W^2}, \tag{5.42}$$

$$\rho \simeq \frac{W}{\pi} \frac{\gamma_j^2}{(\mathscr{E}_j - E)^2 + W^2}. \tag{5.43}$$

In Section 4.2, we used the value [3] $W = 3.36$ MeV for the OMP of [31]. The single-particle reduced width γ_j^2 is approximately given by [48]

$$\gamma_j^2 \simeq 7 \text{ MeV} \tag{5.44}$$

for the average potential of Ross [31] and for $A \simeq 60$. This yields the following value for ρ at $E = \mathscr{E}_j$:

$$\rho_{\max} = \frac{\gamma_j^2}{\pi W} \simeq 0.66, \tag{5.45}$$

which is about the experimental value [4]. Note that Lane [41] takes $W \simeq 1.5$ MeV, $\gamma_j^2 \simeq 5.5$ MeV; in this case, we find $\rho_{\max} \simeq 1.17$, which indicates this value for W is too small by a factor of two. We return to this point below. For $A \simeq 50$–55, ($\mathscr{E}_j - E \simeq 1$ MeV), we obtain from Eq. (5.42):

$$a - a_{sc} \simeq 2.9 \text{ fm}. \tag{5.46}$$

in fair agreement with Fig. 1 and with the value (2.4 fm) determined from the fit of the full curve in Fig. 20.

The "reduction factor" that affects the contribution of the closed channel to the photon width amplitude for $A \simeq 50$–55, and $\epsilon - E = 1$ MeV is given by Eq. (5.34) if, as Lane [41] does, we neglect the dependence of M on κ

$$H \simeq [1 + \kappa(a - a_{sc})]^{-1} \simeq 0.6. \tag{5.47}$$

Lane [41] uses the intermediate coupling model in the R-matrix approach; he introduces level shift functions in Eq. (5.40). From his formula, one finds that the reduction factor for the square of the amplitude is about $\frac{1}{6}$ (for $A \simeq 50$–55, $\epsilon - E = 1$ MeV and when taking $W = 3.36$ MeV rather than [41] $W = 1.5$ MeV, see above). Hence, the reduction factor to the photon width amplitude obtained from Lane's formula is about $(\frac{1}{6})^{1/2} \simeq 0.4$, in fair agreement with the value (5.47). For $A > 60$, Lane [41] finds that the reduction factor in a closed channel remains approximately equal to unity, in agreement with out estimates in Sections 5.7 and 5.8. Hence, the reduction (threshold) factor of the contribution of the closed channels to the photon width amplitudes appears to be about the same in both approaches. It would be of interest to investigate whether this reflects an identical physical interpretation.

5.10. *Discussion*

The entrance channel contribution to the photon width amplitude arises from the external region (Section 5.2). It can dominate the value of the photon width provided that two conditions are fulfilled:

(a) The giant dipole resonance takes away practically all the dipole strength in the internal region (IR). The fulfilment of this condition is in keeping with the schematic model [44] for the GDR. We argued in Section 5.3 that it is not in contradiction with the existence of a sizable external valence capture contribution to the photon width.

(b) The influence of the low-lying closed channels on the external capture amplitude is small. In Sections 5.4–5.9, we investigated this condition, i.e., the contribution of the low-lying excited states to the external capture process. We showed that because of threshold effects, the excited states are small for $A < 60$, but that they become important for $A > 60$. These conclusions are similar to those reached by Lane [40, 41] from a different approach. If one (or more) closed channel gives as large a contribution as the entrance channel to the external capture amplitude, the correlation between neutron and photon widths is expected to disappear. However, this does not necessarily imply that the valence capture model then ceases to give the correct order of magnitude for the photon width.

The results given in [2–4] and in Section 4 (see, e.g., Fig. 3) show that the valence capture contribution to the photon strength function has the same shape as the neutron strength function and thus reaches a maximum near $A = 60$. For $A < 60$, it decreases because the neutron strength function decreases. For $A > 60$, the decrease is slower, because E_γ increases with A. For $A > 60$, however, the role of the closed channels becomes important. Hence, a correlation between neutron and photon widths is not likely to be observed in the regions $A < 40$ and $A > 60$. Moreover, for increasing A, the spectroscopic factor s_f and the level distance D decrease, thereby leading to a corresponding decrease of the valence model value of the photon width.

The fact that the entrance channel contribution to the photon width is nearly independent of energy near threshold (see Figs. 16, 20, and Eq. (5.27)) can be interpreted as follows. A low energy neutron that emerges from a compound nucleus spends a long time in the vicinity of the target nucleus, since its velocity is small. The time spent by the outgoing neutron outside the nucleus (and within the range of the electromagnetic forces) is inversely proportional to its velocity. Therefore, the contribution of the external region to the radiative capture amplitude can be large. Moreover, it is proportional to the escape probability amplitude of the neutron, i.e., to the neutron width, which contains the penetration factor ka. Hence, the product of the two factors is nearly independent of energy. For

$E > 100$ keV, the penetration factor is no longer accurately given by ka and the photon width decreases. Thus, the importance of the entrance channel part of the ER, and thereby the success of the valence capture model, is restricted to low energy and is, in this sense, a threshold effect.

6. Summary and Conclusions

We recall that a brief discussion is given at the end of each section. In Section 2, we relate several parametrizations to one another for the elastic and radiative capture cross sections. We devote particular attention to the fact that the correlation between neutron and photon partial widths depends on the way of describing the potential scattering [13]. However, we show that it is possible to relate the correlation properties in different parametrizations (Section 2.5). These correlations can be calculated from the average scattering matrix (Section 2.4).

In Sections 3.1 and 3.3, we formulate the valence capture model of Lane and Lynn [1–4] in the framework of the shell-model theory of nuclear reactions [5], which is intimately related to Feshbach's theory [6]; we derive several expressions for the resonance parameters and for the background cross section. We discuss the connection between our results and those obtained by Lane and Lynn [1–4] and by Lane and Mughabghab [12] (Sections 3.2, 3.4, and 3.5).

In Section 4, we compute the photon width and the background radiative capture cross section from the valence capture model for $40 < A < 80$. We show that the various expressions derived or recalled in Section 3 yield practically the same results. In particular, the specific choice (Section 4.2) of the average real potential well in the shell-model approach is largely arbitrary, provided that one uses the relations derived in Section 2.5 to refer to a specific parametrization. The calculation of the background cross section (Section 4.4) is somewhat more delicate than that of the photon width (Section 4.3) because it requires an additional dynamical assumption (see Eq. (2.37a) or (2.37b)), which amounts to postulating that the background arises from far-away resonances only (Section 2.7). This might be regarded as a definition of the background cross section; the problem lies in the fact that there is no very clear-cut separation between far-away and close-by resonances. A comparison with experimental data is performed for the cases ^{56}Fe(n, γ) and ^{60}Ni(n, γ).

The numerical results shown in Section 4 are helpful in discussing the conditions of validity of the valence capture model. Section 5 is devoted to the physical, analytical, and numerical investigation of this problem. The following circumstances play an important role in the success of the valence capture model. (a) The giant dipole resonance takes away from the threshold region most of the dipole strength contained in the internal region (Section 5.2). (b) At low energy, a neutron moves slowly in the external region (ER) and thus, has the possibility of emitting a photon. As a consequence of (a) and (b), a low energy neutron usually emits the photon while being in the external region. (c) For $A < 60$, the probability that a neutron emits a photon while being in the closed-channel part of the ER decreases faster than in an open channel when the distance from threshold increases (Sections 5.7–5.9). (d) The probability that the neutron escapes from the compound nucleus to reach the ER in the elastic channel is proportional to the neutron width. Hence, the photon and neutron widths are correlated, for $A < 60$. (e) The photon width presents a maximum near $A = 60$, since it is proportional to the neutron width. (f) The neutron width is proportional to the neutron velocity in the ER because of the penetration factor. The time spent by a neutron in the nearby part of the ER is inversely proportional to its velocity. The photon width is proportional to the product of these two factors and is therefore almost independent of energy in the valence capture model (Sections 4.5.b and 5.7).

Note added in proof. In Figs. 3, 4 and 16, the factor 2π should be replaced by $\pi/2$ on the ordinate scale.

Acknowledgment

We are very grateful to Dr. A. M. Lane for his continuous stimulation. We acknowledge useful discussions with Dr. E. Boridy and with Prof. S. Fallieros. The first author thanks the members of the Division de Physique Théorique at Orsay for their kind hospitality.

References

1. A. M. Lane, *Nucl. Phys.* **11** (1959), 625.
2. A. M. Lane and J. E. Lynn, *Nucl. Phys.* **17** (1960), 563.
3. A. M. Lane and J. E. Lynn, *Nucl. Phys.* **17** (1960), 586.
4. J. E. Lynn, "The Theory of Neutron Resonance Reactions," Clarendon Press, Oxford, 1968.
5. C. Mahaux and H. A. Weidenmüller, "Shell-Model Approach to Nuclear Reactions," North-Holland, Amsterdam, 1969.
6. H. Feshbach, *Ann. Phys. (N.Y.)* **5** (1958), 357.
7. C. Shakin, *Ann. Phys. (N.Y.)* **22** (1963), 54.
8. L. Estrada and H. Feshbach, *Ann. Phys. (N.Y.)* **23** (1963), 123.
9. M. Beer, *Ann. Phys. (N.Y.)* **65** (1971), 181.
10. C. Shakin and M. S. Weiss, *Phys. Rev.* **C2** (1970), 1809.
11. E. Boridy and C. Mahaux, *Nucl. Phys.* **A215** (1973), 605.
12. A. M. Lane and S. F. Mughabghab, *Phys. Rev.* **C10** (1974), 412.
13. H. Feshbach, *in* "Statistical Properties of Nuclei," (J. B. Garg, Ed.), p. 25, Plenum Press, New York, 1972.

14. J. Humblet and L. Rosenfeld, *Nucl. Phys.* **26** (1961), 529.
15. A. M. Lane and R. G. Thomas, *Rev. Mod. Phys.* **30** (1958), 257.
16. E. Boridy and C. Mahaux, *Nucl. Phys.* **A209** (1973), 604.
17. A. M. Lane, *Ann. Phys. (N.Y.)* **63** (1971), 171.
18. C. Bloch, *Nucl. Phys.* **4** (1957), 503.
19. G. E. Brown, *Rev. Mod. Phys.* **31** (1959), 893.
20. J. Hüfner, C. Mahaux, and H. A. Weidenmüller, *Nucl. Phys.* **A105** (1967), 489.
21. C. Mahaux and A. M. Saruis, *Nucl. Phys.* **A138** (1969), 481.
22. E. Boridy and C. Mahaux, *Phys. Letters* **B45** (1973), 81.
23. J. Cugnon and C. Mahaux, *Phys. Rev.* **C10** (1973), 4.
24. H. Feshbach, *Ann. Phys. (N.Y.)* **19** (1962), 287.
25. H. Feshbach, A. K. Kerman, and R. H. Lemmer, *Ann. Phys. (N.Y.)* **41** (1967), 230.
26. H. Feshbach, *Ann. Phys. (N.Y.)* **43** (1967), 410.
27. N. Van Giai and C. Marty, *Nucl. Phys.* **A150** (1970), 593.
28. J. Birkholz, *Nucl. Phys.* **A189** (1972), 385.
29. B. Goulard and J. Joseph, *Canad. J. Phys.* **51** (1973), 2376.
30. R. F. Barrett and T. Terasawa, *Nucl. Phys.* **A240** (1975), 445.
31. A. A. Ross, H. Mark, and R. D. Lawson, *Phys. Rev.* **102** (1956), 1613.
32. P. A. Moldauer, *Nucl. Phys.* **47** (1963), 65.
33. P. A. Jain, *Nucl. Phys.* **50** (1964), 157.
34. H. E. Jackson and E. N. Strait, *Phys. Rev.* **C4** (1971), 1314.
35. J. B. Garg, J. Rainwater, and W. W. Havens, *Phys. Rev.* **C3** (1971), 2447.
36. R. J. Baglan, C. D. Bowman, and B. L. Berman, *Phys. Rev.* **C3** (1971), 672.
37. E. G. Bilpuch, K. K. Seth, C. D. Bowman, R. H. Tabony, R. C. Smith, and H. W. Newson, *Ann. Phys. (N.Y.)* **14** (1961), 387.
38. M. R. Bhat, R. E. Chrien, S. F. Mughabghab, and O. A. Wasson, *in* "Statistical Properties of Nuclei," (J. B. Garg, Ed.), Contribution 4.1, Plenum Press, New York, 1972.
39. J. Cugnon and C. Mahaux, *in* "Proceedings of the Second International Symposium on Neutron Capture Gamma Ray Spectroscopy and Related Topics, Petten, September 2–6, 1974," in press.
40. A. M. Lane, *in* "Proceedings of the International Conference on Photonuclear Reactions and Applications (Asilomar, March 26–30, 1973)," (B. L. Berman, Ed.), Vol. II, p. 803, U.S. Atomic Energy Commission, Office of Information Services, Oak Ridge, Tenn., 1973.
41. A. M. Lane, *Phys. Letters* **B50** (1974), 207.
42. B. Gyarmati, A. M. Lane, and J. Zimányi, *Phys. Letters* **B50** (1974), 316.
43. A. M. Lane, *in* "Proceedings of the Second International Symposium on Neutron Capture Gamma Ray Spectroscopy and Related Topics, Petten, September 2–6, 1974," in press.
44. G. E. Brown and M. Bolsterli, *Phys. Rev. Letters* **3** (1959), 472.
45. A. M. Lane, private communication.
46. R. G. Newton, "Scattering Theory of Waves and Particles," McGraw-Hill, New York, 1966.
47. L. Schäfer, *Nucl. Phys.* **A194** (1972), 497.

Printed by the St Catherine Press Ltd., Tempelhof 37, Bruges, Belgium.